Journal of Sound and Vibration 625 (2026) 119547

Contents lists available at ScienceDirect

Journal of Sound and Vibration

journal homepage: www.elsevier.com/locate/jsvi

Frequency and time domain prediction of railway curve squeal including multiple wheel/rail contact points

Federico Castellini [a,*], Giacomo Squicciarini [b], David Thompson [b], Egidio Di Gialleonardo [a], Roberto Corradi [a]

[a] Department of Mechanical Engineering, Politecnico di Milano, Via Giuseppe La Masa 1, 20156, Milano, Italy
[b] ISVR, University of Southampton, Southampton, SO17 1BJ, United Kingdom

ARTICLE INFO

Keywords:
Curve squeal
Railway noise
Wheel/rail interaction
Tramcar

ABSTRACT

Curve squeal is a high-frequency tonal noise produced by rail vehicles on tight curves, with its occurrence subject to various uncertainties. The generation mechanism is typically attributed to self-excited vibration within the wheel/rail system, with the leading inner wheel of the vehicle often being the most prone to squeal. However, loud and tonal noise is also found to be generated by the outer wheel or for trams when the leading inner wheel is in contact with the grooved rail head. This article presents a wheel/rail interaction model accounting for the presence of multiple contact points between the wheel and the rail. It is used to study the squeal noise generated by a modern low-floor tramcar equipped with resilient wheels. Time-domain simulations are carried out in the case of contact between the flange back of the inner leading wheel and the grooved head. The simulations also reveal that the outer wheel in flange contact can be involved in curve squeal. Variation in the lateral contact point position and the activation of a second contact point on the flange back are found to potentially alter the frequencies involved in the squealing mechanism and the wheel vibration amplitude. A comparison of time-domain simulation results for multiple contact points with full-scale on-track measurements is presented, analysing the inner and outer wheel squeal generated by the tramcar. The squeal is predicted at the same frequencies observed during experiments. Furthermore, the wheel vibration levels in the axial and radial directions are aligned with those measured by accelerometers mounted on the wheels.

1. Introduction

Curve squeal is a loud and annoying tonal noise generated by rail vehicles while negotiating sharp curves. It becomes a serious problem in urban areas, affecting thousands of inhabitants living near the railway and tramway lines. The phenomenon is caused by the self-excited vibration of the wheel that usually occurs at frequencies close to one or more wheel vibration modes [1]. The physical mechanism that triggers this instability is still controversial. The wheel self-excited vibrations were initially attributed to the slip-dependent behaviour of the adhesion coefficient in full sliding [1,2] but self-excited vibrations can also arise in presence of a constant friction coefficient. In this case the friction force acts as a coupling term between the motions in the directions normal and tangential to the contact surface. This mechanism is commonly referred as "mode-coupling instability", where the friction force field modifies the dynamic characteristics of the system, coupling two modes that have natural frequencies close together, resulting in an

* Corresponding author.
E-mail address: federico.castellini@polimi.it (F. Castellini).

https://doi.org/10.1016/j.jsv.2025.119547
Received 21 January 2025; Received in revised form 11 November 2025; Accepted 12 November 2025
Available online 15 November 2025

unstable behaviour of the system [3–6]. The same mechanism can be caused by the coupling between the wheel and the rail dynamics, as highlighted in [7,8]. A thorough literature review of the several experimental and numerical investigations concerning curve squeal is provided by Thompson et al. in [9].

Curve squeal predictions can be carried out using either frequency- or time-domain formulations. In the frequency-domain approach, the system is linearised for small fluctuations of the friction force about the steady-state curving condition and the stability of the linearised system is studied to determine potential unstable frequencies. In the time- domain approach, the nonlinear equations are solved directly with numerical techniques [9]. Frequency-domain formulation was first proposed by Heckl [10,11] and extended by De Beer et al. [12] including the wheel and the rail vibration in vertical and lateral directions. This formulation has been further developed by Huang [13,14] to consider also longitudinal and spin dynamics and by Squicciarini et al. [15–17] to include the simultaneous presence of multiple contact points between the wheel and the rail.

Time-domain formulations involve the integration of the equations of motion that describe the vibration of the wheel/rail coupled model. The wheel and the rail dynamics are included in the coupled model considering their mass, damping and stiffness matrices [13, 18–21] or using Green's functions [22–25]. Several numerical and experimental analyses show that curve squeal develops in the presence of a large angle of attack between the wheel and the rail, resulting in high transverse relative velocity between the two bodies, commonly referred to as creepage when normalized by the rolling velocity. This phenomenon is further amplified by a high value of the friction coefficient [1,22,26]. Some experiments highlight that curve squeal can be effectively mitigated using water or friction modifiers applied on the track [27]. Other test rig experiments reveal that curve squeal may still exist when friction modifiers are applied to eliminate the negative slope in the friction curve [28,29]. This confirms that there are still several uncertainties in the physical mechanism behind the occurrence of squeal. Furthermore, the angle of attack and the friction coefficient are not the only factors that govern the occurrence of the phenomenon. In fact, some analyses highlight that the contact angle and the presence of multiple contact points between the wheel and the rail play a significant role in determining the occurrence of curve squeal events and in promoting the wheel/rail instability at different frequencies. The analysis performed in [30,31] on the curve squeal generated by an articulated tramcar shows that also the leading outer wheel of the vehicle can squeal. Curve squeal was also found on the outer wheel in [32,33]. Furthermore, in the presence of multiple contact points between the wheel and the rail it can be demonstrated, both numerically and experimentally, that flange or flange back contact can alter the squealing frequencies involved in the unstable mechanisms and can promote mode-coupling instability [15–17,34]. The bogie architecture of the vehicle can play an additional crucial role in determining squeal occurrence in sharp curves, as shown in [35]. In this regard, accurate curve squeal prediction requires a precise description of the actual wheel/rail contact conditions and must account in the analysis for potential uncertainties encountered in the field, such as variations in the friction coefficient, track misalignment, wheel/rail profile wear, etc. Since it is usually impractical to include these variations in the curve squeal simulations, which may also vary along the same curve, statistical approaches [15–17] and/or parametric analysis [20,21,23–26] have also been explored to evaluate occurrences of curve squeal.

This paper presents a wheel/rail interaction model that can predict curve squeal in both frequency and time domain. The model accounts for multiple wheel/rail contact points, enabling the analysis of curve squeal occurrences on both the inner and outer wheels. The proposed formulation overcomes the main limitations of the models previously developed by the authors for squeal analysis in the presence of single and multiple contact points [15–17,31,35]. In particular, the model is entirely formulated in state-space form, allowing a stability analysis through Complex Eigenvalue Analysis (CEA). This was not possible in the two-contact points formulation proposed by the authors in [16], where the stability analysis was performed adopting the Nyquist criterion for Multi Input Multi Output (MIMO) systems [36,37]. The previously developed methods did not allow for tracking the eigenvalue evolution as a function of specific wheel/rail contact parameters. Moreover, they required the definition of the wheel and rail FRFs with very small frequency steps, leading to an increase in computational cost, which is higher compared to the CEA-based analysis proposed in the present work. This study also introduces substantial updates regarding time-domain simulations. The simplified approach proposed by Ding [5] has been extended and thoroughly revised to include longitudinal dynamics, rail dynamics, and the presence of a second contact point. The contact force formulation has also been updated by incorporating an unsteady tangential contact model based on Kalker's variational theory [38], as implemented in the CONTACT algorithm [39]. This allows the capture of potential unsteady phenomena occurring in high-frequency wheel/rail contact, in line with previous studies such as those in [21,23] but now also including the effect of a slip-dependent friction coefficient.

The new formulation is used to perform parametric analyses and time-domain simulations on the inner and the outer leading wheels of a modern tramcar, with the focus on the effect of flange contact on curve squeal. While some time-domain simulations of squeal on the outer wheel of conventional railway vehicles have already been presented in [34], squeal on the outer wheel in tramway applications has not yet been thoroughly investigated. Moreover, for the first time in the literature, time-domain simulations of squeal generated by the leading inner wheel in contact with the flange back are presented. An additional novel contribution of this study is the quantitative comparison of the results of the mathematical model against experimental measurements in full-scale tests. In particular, a comparison is made between the outcomes of time-domain simulations and vibration measurements obtained from accelerometers mounted on the wheels of a modern articulated tramcar. Noise levels recorded by trackside microphones are also considered, as these have been employed for the validation of frequency- and time-domain models in previous research. The experimental validation is performed on both inner and outer wheels, enabling the verification of the predicted squeal frequencies and allowing a direct comparison between simulated wheel vibration amplitudes and full-scale measurements collected during squeal events. The article is organised as follows. A description of the bogie curving behaviour is provided in Section 2, highlighting the possible contact conditions that can occur between the wheels and the rails, for either conventional rail vehicles or tramcars. Then, the equations of motion of the wheel and the rail are formulated in Section 3 for curve squeal analysis. A linearized version of the equations of motion is provided to carry out prediction in the frequency domain. Section 4 presents simulation results with focus on time-domain analyses. The reference

situation involves a modern articulated tramcar navigating a sharp curve. Simulations are conducted with single and multiple contact points between the wheel and rail, and all simulations are repeated with varying friction coefficients. The influence of the track gauge, which causes a variation in the normal force on the flange and/or flange back, is evaluated along with that of the lateral position of the contact point. Section 5 provides a comparison between the model results and measurements of curve squeal performed on a tramcar in an urban environment.

2. Steady-state curving behaviour

Curve squeal is strongly related to the wheel/rail contact conditions, which are primarily determined by the vehicle curving behaviour. In modern light rail vehicles, wheelsets (the assembly of the axle and wheels) are typically located within a bogie frame, constrained to remain parallel to each other during rolling. Note that the wheels can either be rigidly connected by a single axle (solid axle arrangement) or free to rotate independently (independently rotating wheels). The quasistatic curving behaviour of each bogie depends on many factors, but particularly on the train speed, the curve radius, the wheel and rail transverse profiles and the cant of the track. At low speed, and in tight radius curves, the leading wheelset runs in flange contact with the outer rail and the trailing wheelset is shifted towards the inner rail (see Fig. 1a). As speed increases (or curve radius increases) the rear wheelset moves outwards, reducing the bogie yaw and the angle of the leading wheelset with respect to the radial direction (i.e. the wheelset angle of attack). Thus, the angle of attack between the leading wheelset and the rail is larger for sharper curves and low speed [1]. Generally, considering a small curve radius, the leading outer wheel of the bogie is in flange contact. The other wheels, despite the presence of a relative lateral displacement and a relative yaw angle with respect to the rail, are in contact at the wheel tread only. This situation is commonly called “free curving”. For a tread contact condition, a single contact point can reasonably describe the wheel/rail interaction. However, when the wheel flange touches the rail gauge face, a second contact point must typically be considered. When running in very narrow curves, the bogie runs in “constrained curving” conditions and the trailing inner wheel is also in flange contact (see Fig. 1b). Moreover, if the tracks are fitted with checkrails or grooved rails, typical of tramways, a second contact point can form at the flange back of the leading inner wheel (see Fig. 1c). As an illustrative example, Fig. 2 shows the possible wheel/rail contact conditions for the leading inner and outer wheels on a left-hand curve.

3. Methodology

The high-frequency interaction between the wheel and rail is studied through two simulation steps. First, the dynamics of the vehicle is simulated to determine steady-state curving conditions using vehicle dynamics multibody software. This analysis considers the physical and geometrical characteristics of the vehicle and track, treating them as rigid bodies, while incorporating the first deformable modes of the axle or rubber elements in resilient wheels [16,40]. This step identifies the behaviour of the bogie and wheelsets along the curve, and gives the contact conditions for each wheel, including contact point position, normal load, contact patch dimensions, creepages, creep forces, contact angle, and the curvature of the wheel and rail profiles near the contact points.

In the second simulation step, a model of a single wheel and track is used to evaluate the high-frequency dynamics. The wheelset vibration modes are decoupled from the rest of the vehicle above 20 Hz by the primary suspensions [1] so only the wheelset is included. The wheel/rail coupled system is analysed by considering the dynamic fluctuation of the contact forces with respect to the steady-state ones, which are balanced by the primary suspensions. The schematic overview of the calculation steps is shown in Fig. 3.

The wheel/rail interaction during rolling is governed by contact forces between the two bodies, coupling their dynamics. In the curve squeal model, the contact problem is solved in two steps: first, computing the normal load at contact points, then solving the tangential problem. This requires expressing contact quantities (velocities, displacements and forces) at contact points. Two sets of local reference systems are therefore introduced for each contact patch (see Fig. 4): one that is oriented as the track reference frame and

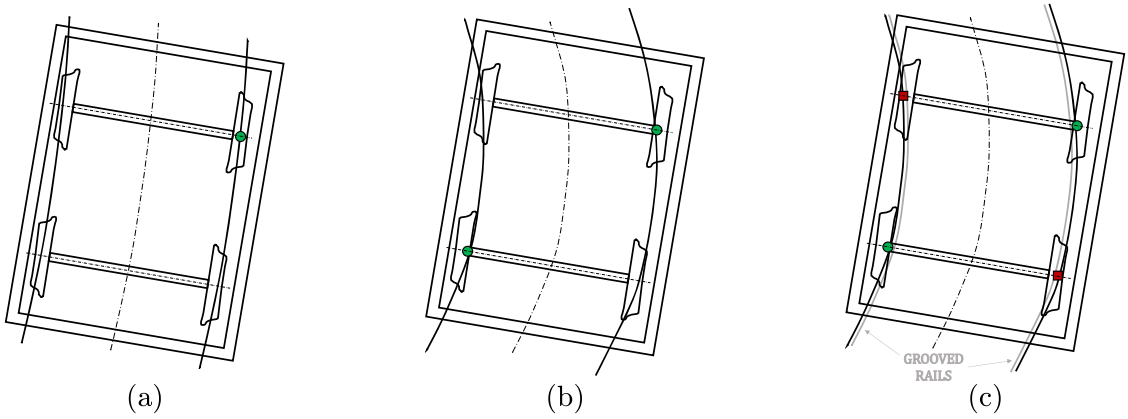

Fig. 1. Curving behaviour of a bogie in curve: (a) large curve radius, free curving, (b) low curve radius, constrained curving and (c) tight curve with grooved rails. Green dots (●) and red squares (■) indicate flange and flange back contacts.

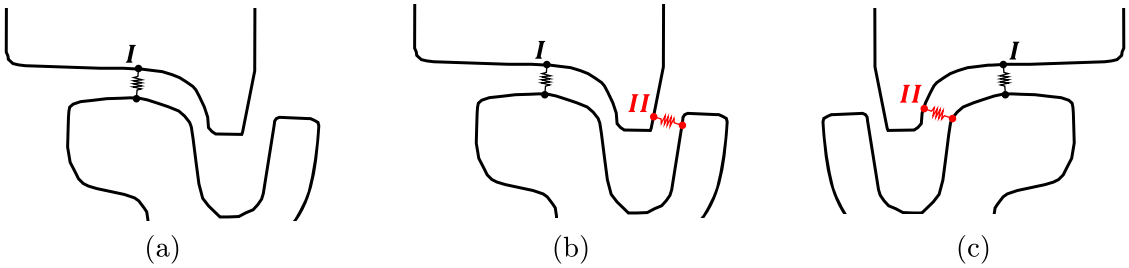

Fig. 2. Overview of the potential wheel/rail contact conditions on the leading axle during a left-hand curve: (a) inner wheel, single contact point on the wheel tread, (b) inner wheel, multiple contacts on the wheel tread and flange back and (c) outer wheel, contacts on the wheel tread and on the wheel flange.

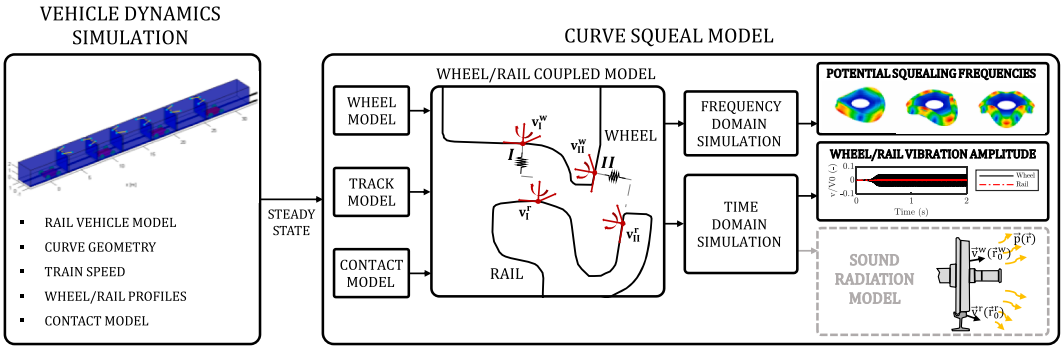

Fig. 3. Schematic overview of the modelling approach.

defines the contact quantities according to the longitudinal, lateral and vertical directions (x,y,z), and another that is oriented (rotated) according to the contact plane (1,2,3) by the contact angle θ. This approach allows the normal and tangential contact problems to be solved at each contact patch, as it enables the evaluation of the relative displacement and velocity of the wheel and the rail in the longitudinal, transverse and normal directions.

The wheel/rail coupled model can be schematized as a MIMO system with feedback loop (see Fig. 5). The time-domain simulation is based on an incremental approach, considering each variable as the sum of the quasi-static quantities obtained from the multibody simulation (steady-state curving conditions) and the dynamic components computed during the integration of the equation of motion of the wheel/rail coupled system. At each time step, the dynamic components of the displacement ($\mathbf{x_w}, \mathbf{x_r}$) and the velocity ($\dot{\mathbf{x}}_\mathbf{w}, \dot{\mathbf{x}}_\mathbf{r}$) of the wheel and the rail are computed by solving the equations of motion related to the wheel and the rail dynamics, written in a state-space form. The model uses a fourth-order Runge Kutta scheme with a fixed time step of 5×10^{-6} s, as it ensures a good trade-off between accuracy and computational cost without introducing artificial damping. The wheel/rail relative displacement in the normal direction at contact points is updated to solve the normal problem. Similarly, the total creepages are computed as the sum of the steady-state and dynamic components. This allows, after solving the normal problem, the tangential problem to be solved by computing the total forces acting between the two bodies (**F**). The dynamic component of these forces (**f**) is then obtained as the

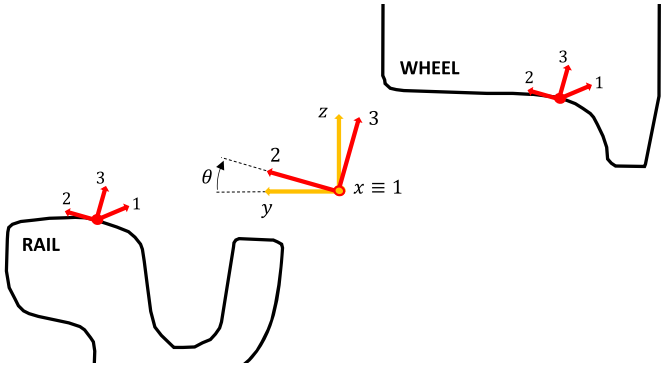

Fig. 4. Schematic representation of the wheel/rail interaction: track (x,y,z) and rotated (1,2,3) contact reference frames.

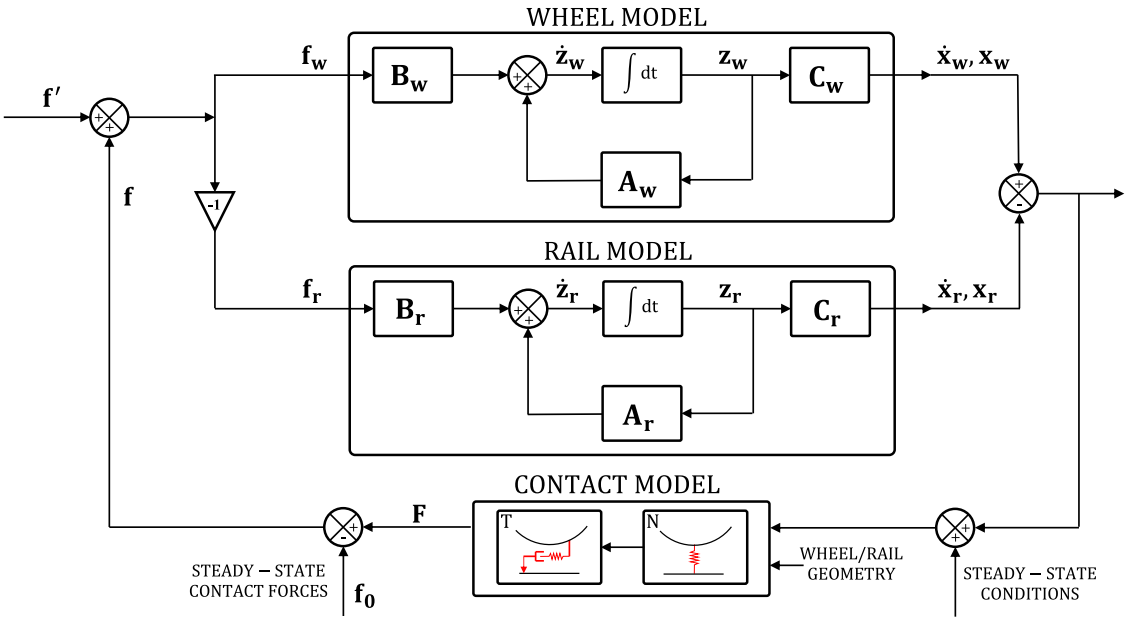

Fig. 5. Schematic representation of the wheel/rail interaction: block diagram of the model adopting a state-space formulation.

difference between the total forces and the steady state ones ($\mathbf{f}_0$) and becomes the input for the next time step. Note that creepages are here computed as the difference between the velocity of the wheel and that of the rail, normalized by the rolling velocity. An external input is required as an initial condition to the curve squeal simulation. Initially, the steady-state parameters are imposed at the wheel/rail contact. A perturbation of 100 N in the wheel/rail transverse contact force ($\mathbf{f}'$) is applied to the steady-state curving condition to analyse the system behaviour after 0.1 s. In the case of a stable system, the perturbation vanishes after a transient. If the system is unstable, the vibration of the wheel and the rail rapidly increases until reaching a limit cycle.

3.1. *Wheel/rail coupled model in state-space form*

The equation of motion of the wheel, written in state-space form and with respect to the x-y-z contact reference system (see Fig. 4) is:

$$\dot{\mathbf{z}}_\mathbf{w} = \mathbf{A_w}\mathbf{z_w} + \mathbf{B_w}\mathbf{f_w} \tag{1}$$

where $\mathbf{z_w} = [\dot{\mathbf{q}}_\mathbf{w}\ \mathbf{q_w}]^\mathrm{T}$ is the vector of the wheel state variables, $\mathbf{A_w}$ is the state matrix of the wheel, $\mathbf{B_w}$ is the input matrix and $\mathbf{f_w}$ is the vector of the forces applied to the wheel at the contact points. A more detailed description of the matrices $\mathbf{A_w}$ and $\mathbf{B_w}$ is given below. The same formulation can be applied to describe the rail dynamics:

$$\dot{\mathbf{z}}_r = \mathbf{A}_r\mathbf{z}_r + \mathbf{B}_r\mathbf{f}_r \tag{2}$$

where $\mathbf{z_r} = [\dot{\mathbf{q}}_\mathbf{r}\ \mathbf{q}_\mathbf{r}]^\mathrm{T}$ is the vector of the rail state variables, $\mathbf{A_r}$ is the state matrix of the rail, $\mathbf{B_r}$ is the input matrix and $\mathbf{f_r}$ is the vector of the forces applied to the rail at the contact points.

The wheel and rail are dynamically coupled through the contact forces. The relationship between the forces applied to the wheel and the rail is given by:

$$\mathbf{f} = \mathbf{f_w} = -\mathbf{f_r} \tag{3}$$

Therefore, the equation of motion of the coupled system is:

$$\dot{\mathbf{z}} = \begin{bmatrix} \dot{\mathbf{z}}_\mathbf{w} \\ \dot{\mathbf{z}}_\mathbf{r} \end{bmatrix} = \begin{bmatrix} \boldsymbol{A}_w & 0 \\ 0 & \boldsymbol{A}_r \end{bmatrix} \begin{bmatrix} \mathbf{z_w} \\ \mathbf{z_r} \end{bmatrix} + \begin{bmatrix} \boldsymbol{B}_w \\ -\boldsymbol{B}_r \end{bmatrix} \mathbf{f} = \mathbf{A}\mathbf{z} + \mathbf{B}\mathbf{f} \tag{4}$$

where $\mathbf{z} = [\mathbf{z_w}\ \mathbf{z_r}]^\mathrm{T}$ collects the state variables of the wheel and the rail and $\mathbf{A}$, $\mathbf{B}$ are the state and input matrices of the coupled system.

3.2. *Wheel/rail interaction in the presence of a single contact point*

The dynamics of the wheel can be introduced though a modal approach, as also performed in [5]. In this article, the wheel dynamics

is directly included by computing the mode shapes matrix at the actual contact positions, as determined from vehicle dynamics simulations. Alternatively, as proposed by [13,18], a rigid roto-translation can also be used to consider the shift in the contact point positions with respect to the nominal ones. The equations of motion of the wheel in modal coordinates can be written as:

$$\mathbf{M}_{qw}\ddot{\mathbf{q}}_{\mathbf{w}} + \mathbf{C}_{qw}\dot{\mathbf{q}}_{\mathbf{w}} + \mathbf{K}_{qw}\mathbf{q}_{\mathbf{w}} = \boldsymbol{\phi}_{w}^{T}\boldsymbol{R}^{T}\mathbf{f}_{\mathbf{w}} \tag{5}$$

where $\mathbf{q}_{\mathbf{w}}$ is the vector of the wheel modal coordinates, $\mathbf{M}_{\mathbf{qw}}, \mathbf{C}_{\mathbf{qw}}, \mathbf{K}_{\mathbf{qw}}$ are the modal mass, damping and stiffness matrices of the wheel and $\boldsymbol{\phi}_{\mathbf{w}} = \left[\phi_{\mathbf{w}}^{(1)}\ \phi_{\mathbf{w}}^{(2)}\ ..\ \phi_{\mathbf{w}}^{(\mathbf{N})}\right]^{\mathrm{T}}$ is the mode shapes matrix considering N modes. In the case of mass normalized modes, the mass, damping and stiffness matrix of the wheel can be written as follows:

$$\begin{aligned}\mathbf{M}_{\mathbf{qw}} &= \mathbf{I}\\ \mathbf{C}_{\mathbf{qw}} &= \mathrm{diag}(2\zeta_{\mathrm{n}}\omega_{\mathrm{n}})\\ \mathbf{K}_{\mathbf{qw}} &= \mathrm{diag}\left(\omega_{\mathrm{n}}^{2}\right)\end{aligned} \tag{6}$$

where ω_{n} and ζ_{n} are the natural circular frequency and the modal damping ratio of the n-th wheel mode. The vectors of the physical coordinates can be obtained as:

$$\mathbf{x}_{\boldsymbol{w}} = \boldsymbol{\phi}_{\mathbf{w}}\mathbf{q}_{\boldsymbol{w}} \tag{7}$$

$$\dot{\mathbf{x}}_{\boldsymbol{w}} = \boldsymbol{\phi}_{\mathbf{w}}\dot{\mathbf{q}}_{\boldsymbol{w}} \tag{8}$$

where $\mathbf{x}_{\mathbf{w}} = [\mathrm{x\ y\ z}\ ]^{\mathrm{T}}$ and $\dot{\mathbf{x}}_{\mathbf{w}} = \left[\mathrm{v_x\ v_y\ v_z}\right]^{\mathrm{T}}$ are the displacement and the velocity vectors of the wheel in longitudinal, lateral and vertical directions at contact points. To solve the contact problem in the normal and tangential directions (see Fig. 4), a rotation matrix $\mathbf{R}(\theta)$ is required:

$$\mathbf{R}(\theta) = \begin{bmatrix} 1 & 0 & 0 \\ 0 & \cos(\theta) & \sin(\theta) \\ 0 & -\sin(\theta) & \cos(\theta) \end{bmatrix} \tag{9}$$

with θ being the contact angle. The dynamic components of the wheel displacement and velocity in the rotated reference frame can be obtained as follows:

$$\mathbf{u}_{\mathbf{w}} = \mathbf{R}\ \mathbf{x}_{\mathbf{w}} \tag{10}$$

$$\dot{\mathbf{u}}_{\mathbf{w}} = \mathbf{R}\ \dot{\mathbf{x}}_{\mathbf{w}} \tag{11}$$

The vectors $\mathbf{u}_{\mathbf{w}} = [\mathrm{u_1\ u_2\ u_3}]^{\mathrm{T}}$ and $\dot{\mathbf{u}}_{\mathbf{w}} = [\mathrm{v_1\ v_2\ v_3}]^{\mathrm{T}}$ collect the physical coordinates in the rotated reference system, where the indexes 1,2,3 refer to the longitudinal, transverse and normal directions.

The equations of motion of the wheel in modal coordinates can be now formulated in state-space form as follows:

$$\dot{\mathbf{z}}_{\mathbf{w}} = \begin{bmatrix} -\mathbf{M}_{\mathbf{qw}}^{-1}\mathbf{C}_{\mathbf{qw}} & -\mathbf{M}_{\mathbf{qw}}^{-1}\mathbf{K}_{\mathbf{qw}} \\ \mathbf{I} & 0 \end{bmatrix}\mathbf{z}_{\mathbf{w}} + \begin{bmatrix} \mathbf{M}_{\mathbf{qw}}^{-1}\boldsymbol{\phi}_{\mathbf{w}}^{\mathbf{T}}\mathbf{R}^{\mathbf{T}} \\ 0 \end{bmatrix}\mathbf{f}_{\mathbf{w}} = \mathbf{A}_{\mathbf{w}}\mathbf{z}_{\mathbf{w}} + \mathbf{B}_{\mathbf{w}}\mathbf{f}_{\mathbf{w}} \tag{12}$$

where the vector $\mathbf{f}_{\mathbf{w}}$ collects the wheel/rail contact forces (longitudinal, transverse and normal) which are expressed with respect to the rotated reference system and are oriented normally and tangentially to the contact plane.

Different strategies can be adopted to include the rail dynamics in the time-domain simulations. Some previous works rely on the use of Green's functions [22–25] while others use a ratio of polynomials with coefficients obtained by best-fitting the rail frequency response functions [16,18]. The track can also be modelled using Finite Element (FE) methods [20]. However, the direct time integration of a track FE model requires a significant computational effort which may dramatically affect the computation time. The analysis carried out by Ding et al. [7] highlights that the only significant effect of the rail dynamics on curve squeal prediction is related to the "damping-like" behaviour of the rail at high frequency, which may lead to instability due to a "coupling-like" mechanism between the wheel and the rail. Similar results were highlighted by Lai et al. in [8]. These findings suggest that a rather simple track model can be adopted to carry out curve squeal prediction, without the need of including rail cross-section deformation, pinned–pinned resonances, or the effect of multiple wheels. Even though the rail considered in this paper is a grooved rail rather than a Vignole rail as in [7], it is reasonable to assume that similar considerations apply, since, as reported in [41], the high-frequency dynamic behaviour of a grooved rail is comparable to that of a Vignole rail. Since the impact of the rail dynamics is not the focus of this investigation, a simplified approach is adopted here, consisting of best-fitting the rail frequency response function from measurements and analytical models through a modal approach. This strategy was also proposed in [18] and can be also applied to fitting advanced models of the track in frequency domain. The model accounts only for the direct terms, neglecting the cross-coupling between the longitudinal, lateral, and vertical components. This formulation results in an equivalent modal model that can be included in the state-space formulation of the coupled system (see Eq. (4)). Thus, the equations of motion of the rail in state space-form can be written in a similar form as the wheel ones (see Eq. (12)).

$$\dot{\mathbf{z}}_\mathbf{r} = \begin{bmatrix} -\mathbf{M}_{\mathbf{qr}}^{-1}\mathbf{C}_{\mathbf{qr}} & -\mathbf{M}_{\mathbf{qr}}^{-1}\mathbf{K}_{\mathbf{qr}} \\ \mathbf{I} & 0 \end{bmatrix} \mathbf{z}_\mathbf{r} + \begin{bmatrix} \mathbf{M}_{\mathbf{qr}}^{-1}\boldsymbol{\phi}_\mathbf{r}^{\mathbf{T}}\mathbf{R}^{\mathbf{T}} \\ 0 \end{bmatrix} \mathbf{f}_\mathbf{r} = \mathbf{A}_\mathbf{r}\mathbf{z}_\mathbf{r} + \mathbf{B}_\mathbf{r}\mathbf{f}_\mathbf{r} \tag{13}$$

3.3. Wheel/rail interaction in the presence of multiple contact points

The formulation introduced in Section 3.2 is now extended to consider the simultaneous presence of multiple contact points. The mode shape matrices of the wheel and rail are reformulated including the mode shapes at the second contact point:

$$\boldsymbol{\phi}_\mathbf{w} = \begin{bmatrix} \boldsymbol{\phi}_\mathbf{w}^{\mathbf{I}} \\ \boldsymbol{\phi}_\mathbf{w}^{\mathbf{II}} \end{bmatrix} \tag{14}$$

$$\boldsymbol{\phi}_\mathbf{r} = \begin{bmatrix} \boldsymbol{\phi}_\mathbf{r}^{\mathbf{I}} \\ \boldsymbol{\phi}_\mathbf{r}^{\mathbf{II}} \end{bmatrix} \tag{15}$$

Displacements $\mathbf{x}_\mathbf{w}^{(i)}$, $\mathbf{x}_\mathbf{r}^{(i)}$ and velocities $\dot{\mathbf{x}}_\mathbf{w}^{(i)}, \dot{\mathbf{x}}_\mathbf{r}^{(i)}$ associated to the i-th contact point (i = I,II) can be computed adopting the transformation from modal to physical coordinate, as shown in Eqs. (7) and (8). Similarly, the rotation matrix accounts for the presence of the second contact point:

$$\mathbf{R} = \begin{bmatrix} \mathbf{R}_\mathbf{I} & \boldsymbol{0} \\ \boldsymbol{0} & \mathbf{R}_\mathbf{II} \end{bmatrix} \tag{16}$$

The equations of motion of the coupled system in state-space form (Eq. (4)) can be then updated. The matrices $\boldsymbol{A_w}$ and $\boldsymbol{A_r}$ are the same as in Eqs. (12) and (13) while the input matrices $\boldsymbol{B_w}$ and $\boldsymbol{B_r}$ include the effect of a second contact point between the wheel and the rail considering the mode shape and the rotation matrices defined in Eqs. (14), (15) and (16).

3.4. Contact model

Normal contact forces are here introduced assuming Hertzian contact between the wheel and the rail [42]. The normal problem is solved knowing the virtual penetration between the wheel and the rail ($\delta^{(\mathrm{I})}, \delta^{(\mathrm{II})}$) and their local curvatures at the contact points obtained from a multibody simulation of the vehicle in the curve [40,43]. In the time-domain simulations, the total penetration at each contact patch is computed as the sum of the steady-state penetration ($\delta_0^{(i)}$) during curving and its dynamic component, which is updated at each time step using the wheel/rail interaction model.

$$\delta^{(\mathrm{i})} = \delta_0^{(\mathrm{i})} - \left(\mathrm{u}_{3,\mathrm{w}}^{(\mathrm{i})} - \mathrm{u}_{3,\mathrm{r}}^{(\mathrm{i})}\right) \qquad \mathrm{i} = \mathrm{I}, \mathrm{II} \tag{17}$$

The total normal load at each contact point is computed with the Hertzian theory as:

$$\mathrm{F}_3^{(\mathrm{i})} = \mathrm{C}_H^{(i)} \left(\delta^{(i)}\right)^{3/2} \qquad \mathrm{i} = \mathrm{I}, \mathrm{II} \tag{18}$$

where $\delta^{(\mathrm{i})}$ is the virtual penetration between the wheel and the rail at contact and $\mathrm{C}_H^{(i)}$ depends on the local radii of curvature of the bodies in contact and their material properties [1,38]. Analogously, the total creepages on each contact point are computed as the sum of the steady state creepages (from vehicle dynamics simulation) and their dynamic components:

$$\gamma_j^{(\mathrm{i})} = \gamma_{\mathrm{j0}}^{(\mathrm{i})} + \frac{1}{V_0}\left(\dot{u}_{j,w}^{(i)} - \dot{u}_{j,r}^{(i)}\right) \qquad \mathrm{i} = \mathrm{I}, \mathrm{II} \quad \mathrm{j} = 1, 2 \tag{19}$$

Since the normal problem is solved using the Hertzian approach, the total tangential forces acting between the two bodies are calculated based on the total creepages, the total normal load and the geometry of the contact patch. The dynamic component of the wheel/rail contact forces $\mathrm{f}_j^{(\mathrm{i})}$ is finally computed as the difference between the total forces $\mathrm{F}_j^{(\mathrm{i})}$ and the steady state ones $\mathrm{f}_{\mathrm{j0}}^{(\mathrm{i})}$ and becomes the new input of the wheel/rail coupled model (see Fig. 5):

$$\mathrm{f}_j^{(\mathrm{i})} = \mathrm{F}_j^{(\mathrm{i})} - \mathrm{f}_{\mathrm{j0}}^{(\mathrm{i})} \qquad \mathrm{i} = \mathrm{I}, \mathrm{II} \quad \mathrm{j} = 1, 2, 3 \tag{20}$$

Several theories are available to solve the tangential problem [38,44–47]. In this work, Kalker's variational theory is used. This is addressed with the CONTACT software, employing exclusively the TangGC algorithm (see [39]). It allows the inclusion of transient effects in time-domain simulations and incorporates the heuristic formula to introduce a slip-dependent (kinetic) friction coefficient μ_k proposed by Polach in [45]:

$$\mu_k(\gamma) = \mu_0\left(\left(1 - \mathrm{A_{ff}}\right)\mathrm{e}^{-\mathrm{B_{ff}}V_0\gamma} + \mathrm{A_{ff}}\right) \tag{21}$$

where μ_0 is the static friction coefficient, V_0 is the rolling velocity, γ is the total creepage ($\gamma = \sqrt{\gamma_1^2 + \gamma_2^2}$), with γ_1 and γ_2 being the longitudinal and the transverse creepages, respectively. $\mathrm{A_{ff}}$ and $\mathrm{B_{ff}}$ are the coefficients that define the slope of the slip-dependent part of

the friction curve. They were obtained in [45] by comparing the results of the numerical model against a friction law measured on site. In the simulations carried out in this article, the values estimated for dry rails are employed ($A_{ff} = 0.4$, $B_{ff} = 0.6$). The non-dimensional friction forces (also defined as adhesion coefficient, expressed as the ratio between the tangential forces and the normal load) in the tangential plane are plotted against the longitudinal, transverse and spin creepages in Fig. 6 (μ_0=0.45). One creepage is varied at a time, while others are set to zero. Adhesion curves are generated using the "steady" version of the tangential CONTACT algorithm (see [39]). The normal load is set to 25.9 kN, while the semi-axes of the contact ellipse are 41 mm and 32 mm in the longitudinal and transverse directions, respectively. These data are obtained from vehicle dynamics simulations of the tramcar analysed in this study, considering the leading inner wheel of the second car. Note that the curves shown below are provided as illustrative examples to show the impact of the slip-dependent friction coefficient on the adhesion coefficient. In the time-domain simulations, however, the normal and tangential contact problems are solved at each time step using the "unsteady" version of the tangential CONTACT algorithm.

3.5. Linearized wheel/rail coupled model and stability analysis

A prediction of curve squeal occurrence can be performed by analysing the stability of the system in the frequency domain through Complex Eigenvalue Analysis (CEA). Whereas the full non-linear model is employed in the time-domain simulations, the CEA necessitates linearizing the equations of motion about the steady-state curving condition of the vehicle. As a first step, the linearized expression of the wheel/rail contact forces is needed. For small vibrations about steady-state conditions, the dynamic fluctuation of the normal load can be expressed as the product of the relative displacement between the wheel and the rail in normal direction and the linearized Hertzian contact stiffnesses $k_H^{(I)}$ and $k_H^{(II)}$ [42]:

$$f_3^{(i)} = -k_H^{(i)}\left(u_{3,w}^{(i)} - u_{3,r}^{(i)}\right) \qquad i = I, II \tag{22}$$

The fluctuation in the creep forces can be computed by linearizing the non-linear force-creep relationships:

$$f_j^{(i)} \approx \left[\mu_j\left(\gamma_{j0}^{(i)}, f_{30}^{(i)}\right) + \left.\frac{\partial \mu_j^{(i)}}{\partial F_3^{(i)}}\right|_0 f_{30}^{(i)}\right] f_3^{(i)} + \sum_k \left.\frac{\partial \mu_j^{(i)}}{\partial \gamma_k^{(i)}}\right|_0 \frac{f_{30}^{(i)}}{V_0}\left(v_{k,w}^{(i)} - v_{k,r}^{(i)}\right) = \alpha_j^{(i)} f_3^{(i)} + \sum_k \beta_{jk}^{(i)}\left(v_{k,w}^{(i)} - v_{k,r}^{(i)}\right) \qquad i = I, II \qquad j, k = 1, 2 \tag{23}$$

where $\gamma_{j0}^{(i)}$ and $f_{30}^{(i)}$ are the steady-state creepages and the normal loads associated with the i-th contact point. In this study, the coefficients $\alpha_j^{(i)}$and $\beta_{jk}^{(i)}$ are determined using finite differences, since CONTACT is a numerical model. Alternatively, they can be calculated analytically, when analytical contact models are adopted (e.g., Shen-Hedrick-Elkins [46], Polach [44,45]).

Combining Eqs. (22) and (23) and adopting a matrix notation it is possible to express the vector of the normal and tangential contact forces as a function of the wheel/rail state vector as follows:

$$\mathbf{f} = \begin{bmatrix} f_1 \\ f_2 \\ f_3 \end{bmatrix} = [\boldsymbol{\beta} \quad \boldsymbol{\alpha}] \begin{bmatrix} \mathbf{R} & \mathbf{0} \\ \mathbf{0} & \mathbf{R} \end{bmatrix} [\mathbf{C_w} \quad -\mathbf{C_r}] \begin{bmatrix} \mathbf{z_w} \\ \mathbf{z_r} \end{bmatrix} = \boldsymbol{\Gamma}\mathbf{z} \tag{24}$$

where $\boldsymbol{\alpha}$ and $\boldsymbol{\beta}$ are defined as:

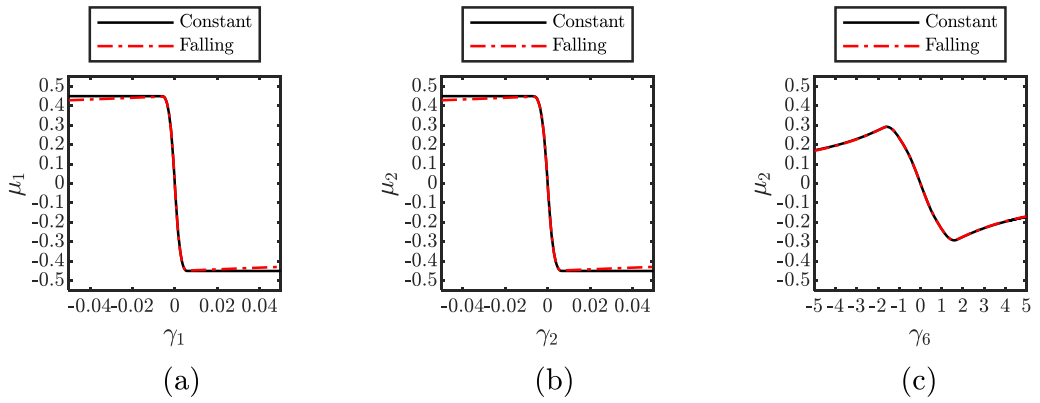

Fig. 6. Adhesion coefficient in (a) longitudinal and (b)(c) transverse direction varying longitudinal, transverse and spin creepages (μ_0=0.45). (▬) Constant friction coefficient and (---) Polach's falling friction model [45].

$$\boldsymbol{\beta} = \begin{bmatrix} \beta_{11} & \beta_{12} & 0 \\ \beta_{21} & \beta_{22} & 0 \\ 0 & 0 & 0 \end{bmatrix} \tag{25}$$

$$\boldsymbol{\alpha} = \begin{bmatrix} 0 & 0 & -k_H\alpha_1 \\ 0 & 0 & -k_H\alpha_2 \\ 0 & 0 & -k_H \end{bmatrix} \tag{26}$$

while $\mathbf{R}$ is the rotation matrix and $\mathbf{C_w}$ and $\mathbf{C_r}$ are the wheel and rail output matrices defined as follows:

$$\mathbf{C_w} = \begin{bmatrix} \boldsymbol{\phi}_w & \mathbf{0} \\ \mathbf{0} & \boldsymbol{\phi}_w \end{bmatrix} \tag{27}$$

$$\mathbf{C_r} = \begin{bmatrix} \boldsymbol{\phi}_r & \mathbf{0} \\ \mathbf{0} & \boldsymbol{\phi}_r \end{bmatrix} \tag{28}$$

The state-space equation of motion of the system (see Eq. (4)) can be rearranged by including the linearized formulation of the contact forces obtained in Eq. (24):

$$\dot{\mathbf{z}} = \mathbf{A}\mathbf{z} + \boldsymbol{B}\boldsymbol{\Gamma}\mathbf{z} = \left(\mathbf{A} + \mathbf{A_f}\right)\mathbf{z} = \widetilde{\mathbf{A}}\mathbf{z} \tag{29}$$

The state-space matrix of the wheel/rail system, which includes the effect of the contact forces $\widetilde{\mathbf{A}}$, is thus obtained. The stability of the coupled wheel/rail system is governed by the eigenvalues of the matrix $\widetilde{\mathbf{A}}$. The sign of their real part indicates whether the system is unstable and helps identify the possible vibration modes involved in the unstable mechanism.

The formulation can be extended to the case of multiple contact points by considering the rotation matrix $\mathbf{R}$ defined in Eq. (16) and the mode shape matrices $\boldsymbol{\phi}_w, \boldsymbol{\phi}_r$ including the terms associated with the second contact point (see Eqs. (14) and (15)) and by expanding the matrices $\boldsymbol{\alpha}$ and $\boldsymbol{\beta}$ as follows:

$$\boldsymbol{\beta} = \begin{bmatrix} \boldsymbol{\beta}_I & \mathbf{0} \\ \mathbf{0} & \boldsymbol{\beta}_{II} \end{bmatrix} \tag{30}$$

$$\boldsymbol{\alpha} = \begin{bmatrix} \boldsymbol{\alpha}_I & \mathbf{0} \\ \mathbf{0} & \boldsymbol{\alpha}_{II} \end{bmatrix} \tag{31}$$

where $\boldsymbol{\alpha}_i$ and $\boldsymbol{\beta}_i$ ($i = I, II$) can be defined combining Eq. (23), Eqs. (25) and (26) for the i-th contact point.

4. Results of numerical simulations

This section analyses curve squeal generated by a modern low-floor tramcar. The description of the simulated cases with reference to vehicle dynamics simulations are presented in Section 4.1. The simulations of curve squeal on the inner wheel are described in Sections 4.2 and Section 4.3 while those on the outer wheel are presented in Section 4.4. The parameters of the wheel and rail modal models are calibrated using experimental data, including Experimental Modal Analysis (EMA) of the resilient wheel and impact testing on the tramway track with grooved rails (see Appendix B for more details).

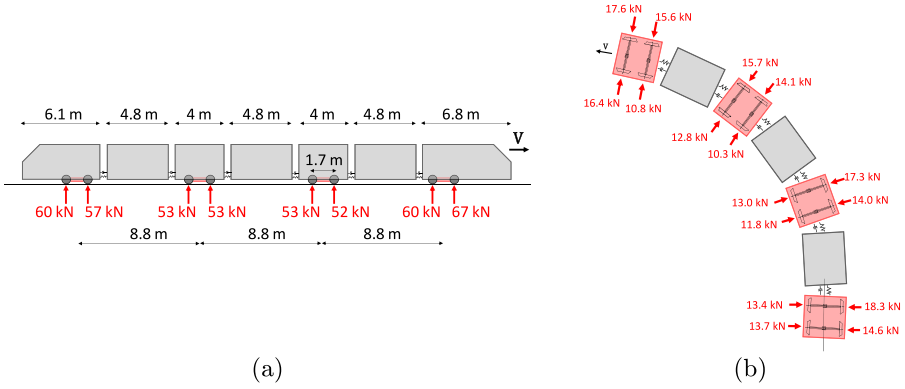

Fig. 7. Schematic representation of the tramcar: (a) geometry, axle load and (b) lateral forces (μ_0=0.45 and track gauge 1445 mm) in steady state curving condition derived from multibody simulations.

4.1. Vehicle dynamics simulations

The results focus on squeal noise generated by a modern articulated tramcar running at 10 km/h on a curve with radius R = 17.5 m. The tramcar is equipped with resilient wheels that rotate independently. It is the same tramcar also analysed in [16,17,31]. The vehicle consists of seven cars, three of which are suspended between those equipped with bogies. The multibody model of the tramcar is developed using an in-house vehicle dynamics software specifically designed to simulate the dynamic behaviour of a tramcar on both tangent and curved tracks, accounting for large displacements and the resulting kinematic nonlinearities [40,43,48,49]. Carbodies are modelled as rigid bodies while the flexibility of wheelsets and bogie frames, as well as the presence of resilient wheels, is considered. The modules are interconnected via kinematic constraints and/or elastic and damping elements, replicating the real mechanical connections between carbodies. The system's equations of motion are expressed in terms of generalized coordinates, which allows to include both rigid body motions and flexible modes of each component such as the deformability of the resilient wheels. The wheel–rail contact model is suitable for capturing the typical contact conditions observed in tram operation. It accounts for out of plane contacts due to significant angles of attack in tight curves, and the potential occurrence of multiple contact points on both the tread and flange. The wheel/rail contact model is based on a multi-Hertzian approach [50,51] that enables the possibility of multiple simultaneous contact points. FASTSIM algorithm is adopted to compute the tangential forces [47]. A schematic representation of the geometry of the vehicle, the axle loads and the steady-state lateral forces on each wheel are reported in Fig. 7.

The analysis focuses on the leading wheels of the second bogie of the tramcar. This allows for the comparison of the numerical results with a set of vibration measurements performed by installing accelerometers on the leading inner and outer wheels of that bogie during the negotiation of the curve (see Section 5 and [30,31]). Nevertheless, the curving conditions of the other bogies in curve are comparable because they share the same geometry, they have similar axle loads and distribution of steady-state lateral forces (see Fig. 7).

Several experiments have been performed on this tramcar over the last decade, analysing its behaviour in sharp curves. The presence of contact between the flange back of the inner leading wheel and the grooved head was also observed. Furthermore, squeal was detected on both the inner and outer wheels under different contact conditions [27,30,31]. The analyses conducted in [16,31] also show an intermittent behaviour of curve squeal during curve negotiation, attributed to a variation in the wheel/rail contact conditions along the curve. Thus, similarly to what was presented in [16], the effect of flange back contact on curve squeal is assessed here by modifying the track gauge in the multibody simulations. This is varied from its nominal value of 1445 mm to 1450 mm. This numerical exercise allows the effects of misalignment along the track to be explored in a simplified manner using the multibody approach. Additionally, simulations are repeated with different values of the nominal friction coefficient (μ_0=0.15, μ_0=0.30, μ_0=0.45 and μ_0=0.60). It is observed that the contact between the flange back and the grooved rail head is activated with a track gauge of 1446 mm for μ_0=0.60 or higher. The normal load on the flange back of the inner wheel is found to increase with both track gauge and friction coefficient. The cases analysed in the following Sections are listed in Table 1. Additional details on the wheel–rail contact parameters adopted for each simulated case are provided in Appendix A. First, the model is used to study the more conventional situation in which there is a single contact point between the wheel tread and the top of the rail (case a). Then, simulations with multiple contact points

Table 1
Overview of the numerical simulations.

Case	Wheel (CP*)	Vehicle Dynamics Simulations	W/R Contact
(a)	Inner Wheel (I: top of the rail)	Friction coefficient (0.15–0.6) Track gauge (1445) Number of MB** simulations: 4	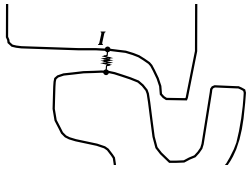
(b)	Inner Wheel (I: rail, II: grooved head)	Friction coefficient (0.15–0.6) Track gauge (1446–1450) Number of MB** simulations: 20	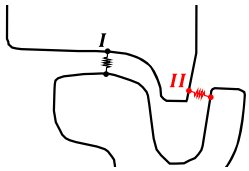
(c)	Outer Wheel (I: rail, II: gauge face)	Friction coefficient (0.15–0.6) Track gauge (1445–1450) Number of MB** simulations: 24	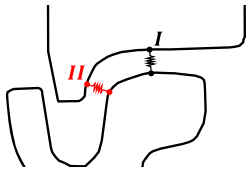

* CP: Contact Points.
** MB: Multibody Simulations.

are carried out considering both the leading inner and the outer wheels (case b and case c, respectively). All the simulations are carried out including the falling friction effect as presented in Eq. (21) (A_{ff}=0.4, B_{ff}=0.6).

The simulations are performed considering nominal conditions for both wheel and rail profiles (see Fig. 8). While this assumption provides a consistent baseline, it does not fully reflect the actual conditions typically encountered in tramway operation, where rail maintenance activities are much less frequent and a significant level of rail wear is often present, as also observed during on-track tests. Even minor alterations in profile geometry due to wear can cause appreciable shifts in the wheel/rail contact location, particularly on the tread, which may substantially influence dynamic behaviour. In fact, relying solely on nominal contact point location can lead to an underestimation or an overestimation of squeal occurrence, as relatively small changes may be sufficient to induce a transition from stable to unstable conditions or to activate the instability of different modes (as shown in [1,12,21,23–25]). To account for this effect, a parametric analysis is conducted for each scenario obtained from vehicle dynamics simulations, by varying the lateral position of the contact points.

4.2. Case a: curve squeal on the leading inner wheel in the presence of a single contact point

In this section, the results of the squeal simulations in the case of a single contact point between the leading inner wheel and the rail are presented. The steady-state values of creepages and normal load are obtained from the multibody simulation with track gauge 1445 mm. The friction coefficient is varied according to the multibody simulations with μ_0=0.15, μ_0=0.30, μ_0=0.45 and μ_0=0.60. Frequency and time domain simulations are carried out to identify the potential unstable frequencies for each analysed case and to determine the wheel modes that dominate the limit cycle. The lateral contact position on the wheel tread $Y_w^{(I)}$ is varied between 0 and 25 mm. The system is unstable starting at $Y_w^{(I)}$=0 mm for $\mu_0 = 0.45$ or higher. As also reported in [1,21,23], the system is more prone to squeal when the contact point shifts laterally towards the outer part of the wheel tread. For $Y_w^{(I)}$ higher than 10 mm, unstable conditions are obtained also for $\mu_0 = 0.30$. Squeal is found at 535 Hz corresponding to the natural frequency of the wheel axial mode with 2 ND. This is also the squealing frequency predicted through the Complex Eigenvalue Analysis (CEA). The results of the simulation performed with friction coefficient $\mu_0 = 0.45$ and Y_w^I =22 mm (the nominal contact point position on the wheel, see Fig. 8a) are here analysed in detail. The axial and radial vibration velocity of the wheel in proximity to the contact point is reported in Fig. 9a. Results are normalized against the vehicle speed V_0. A 5 ms time window zoom is also provided to better highlight the amplitude of the wheel vibration during the limit cycle. Similar results in terms of wheel vibration and contact force amplitudes can be found in [21,23,26].

The tonal nature of curve squeal is shown in Fig. 9b where the spectrograms of the wheel vibration velocity in axial and radial directions is reported. Higher-order harmonics are also visible in the spectrogram due to the non-linearities in the normal and tangential contact problems. The amplitude of the wheel vibration in the axial direction is much higher than that of the rail (see Fig. 9a). This is because the wheel mobility is higher than the one of the track at this frequency. Although they are not reported here for brevity, similar results are obtained in simulations with different friction coefficients or lateral positions of the contact point on the wheel.

4.3. Case b: curve squeal on the leading inner wheel in the presence of multiple contact points

In this section, curve squeal of the leading inner wheel is analysed in the presence of a contact point between the wheel flange back and the grooved head. This wheel/rail contact condition has already been observed in [16,27,30]. This condition is favoured by the

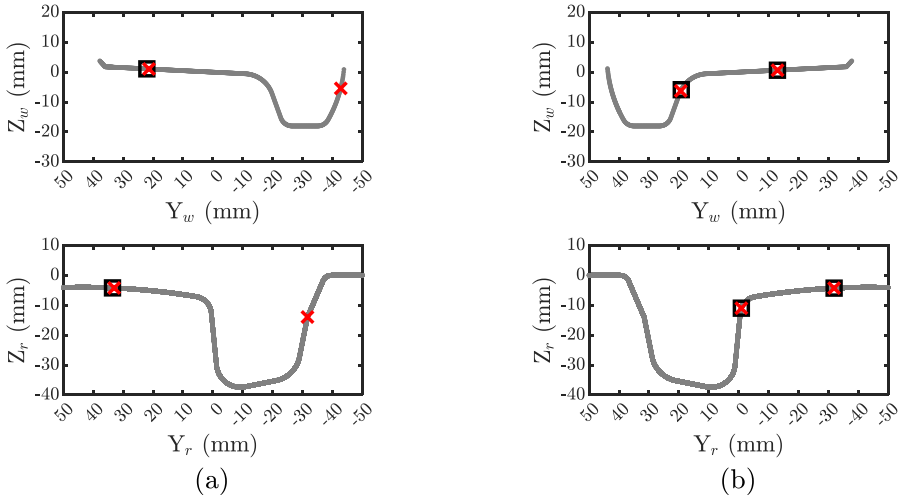

Fig. 8. Wheel and rail profiles used in the vehicle dynamics simulations (μ_0=0.45) and nominal position of the contact points: (a) inner wheel and (b) outer wheel (□ track gauge 1445 mm, ✗ track gauge 1447 mm).

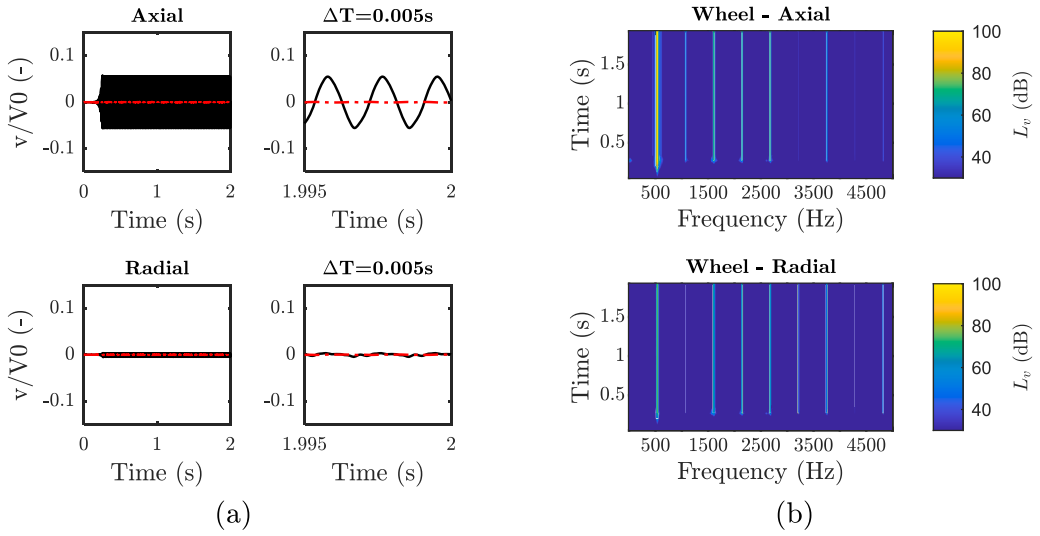

Fig. 9. Curve squeal on the inner wheel in the presence of single contact point for $\mu_0 = 0.45$, track gauge 1445 mm and $Y_w^{(I)}$=22 mm: (a) time evolution of (▬) wheel and (---) rail vibration and (b) spectra of wheel axial and radial fluctuation (dB, re 10^{-6} m/s).

deformability of the rubber elements of the resilient wheels but can also be promoted by significant wear of the wheel/rail profiles or track misalignment [16]. A schematic representation of the wheel/rail contact conditions in the presence of a flange back contact was shown in Fig. 2b Analogously to the previous section, each case is analysed considering variability in the lateral contact point position on the tread. Increasing the track gauge reduces the clearance between the wheel flange back and the grooved head, allowing a flange back contact to occur with lower values of lateral relative displacement and yaw angle between the wheel and the rail. Furthermore, higher values of the friction coefficient generate a greater transverse creep force, which is directed outward. This increased force causes an increase in the lateral deformation of the rubber elements within the resilient wheels, resulting in an additional relative lateral displacement between the wheels and the rails which facilitates the activation of the flange back contact on the leading inner wheels. These contact conditions, as also shown by the frequency-domain analysis in [16], promote the instability of wheel modes at 1500 Hz and 2500 Hz, which are characterized by strong axial/radial dynamic coupling. As the real parts of the two eigenvalues are very close, either of them can potentially dominate the limit cycle response during squealing events. In this case, it is found that the position of the contact point on the tread plays a determining role, together with the effect of the track gauge (and thus the flange load), in defining the system's squeal frequency. Specifically, it is observed that when the contact point position on the tread is external ($Y_w^{(I)}$

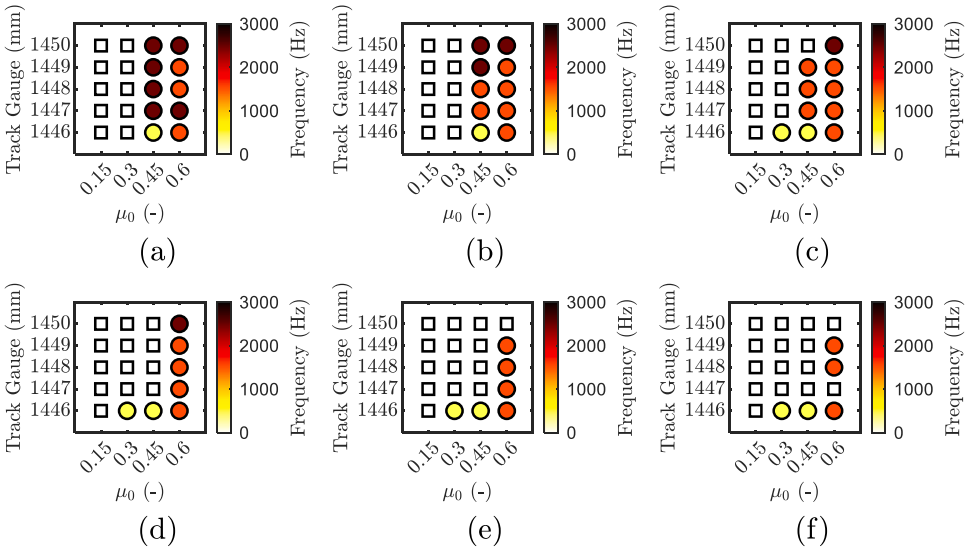

Fig. 10. Squealing frequencies varying the friction coefficient and the track gauge for different lateral contact point positions on the tread $Y_w^{(I)}$ of the inner wheel: (a) $Y_w^{(I)} = 0$ mm, (b) $Y_w^{(I)} = 5$ mm, (c) $Y_w^{(I)} = 10$ mm, (d) $Y_w^{(I)} = 15$ mm, (e) $Y_w^{(I)} = 20$ mm and (f) $Y_w^{(I)} = 25$ mm. Square marks (□) indicate stable system.

higher than 5 mm), instability tends to occur around 1500 Hz, whereas when the contact point is more internal ($Y_w^{(I)}$ lower than 5 mm), keeping all other contact parameters equal, squeal is generated around 2500 Hz. The effect of increased gauge (and, as mentioned above, the increased normal load on the flange back) appears to further promote instability at 2500 Hz, which is also observed for $Y_w^{(I)}$ = 15 mm, but only for a track gauge of 1450 mm. The impact of varying the contact position on the flange back $Y_w^{(II)}$ is not reported here since it does not have a relevant effect on the squealing frequencies and vibration amplitude. An overview of the simulation results varying the friction coefficient, gauge, and contact point position on the wheel is shown in Fig. 10, where the squeal frequencies obtained by performing frequency- and time-domain simulations for each analysed scenario are reported. Also in this case, the dominant limit cycle frequency matches the results from the Complex Eigenvalue Analysis (CEA). In particular, it is observed that, in cases with two unstable modes, the dominant squealing frequency corresponds to the eigenvalue with the highest real part. In the simulations with two contact points, no positive real part is found for $\mu_0 = 0.15$ and $\mu_0 = 0.30$.

Two contact conditions leading to squeal at different frequencies are now analysed in detail. Fig. 11 examines the wheel vibration in the case of squeal at 1550 Hz ($\mu_0 = 0.6$, track gauge 1447 mm, and $Y_w^{(I)} = 21$ mm). Once again, the tonal behaviour typical of curve squeal is observed. Unlike the case of squeal at 535 Hz, a significant radial vibration is present, which exceeds the axial component. This behaviour is due to the strong axial/radial coupling of the 3 ND wheel vibration modes, which is also evident when examining the wheel mobility plot in both directions around 1500 Hz (see Appendix B). As in the previous case, the vibration amplitude of the rail is significantly lower than that of the wheel.

In the squeal simulation at 2500 Hz ($\mu_0 = 0.6$, track gauge 1450 mm, and $Y_w^{(I)} = 15$ mm, see Fig. 12), a behaviour similar to that observed in Fig. 11 is detected. Also in this case, the axial/radial coupling of the modes involved in the system instability is significant and generates considerable vibration in both directions.

4.4. Case c: curve squeal on the leading outer wheel

The behaviour of the outer wheel is analysed in this subsection. Also in this case, a series of simulations was carried out by varying the track gauge, the friction coefficient, and the position of the wheel/rail contact point on the tread. The outer wheel is always in a multiple contact point condition, with one contact point on the tread and one on the flange (see Fig. 2c). Unlike the inner wheel, where the presence of two contact points can lead to different outcomes, the simulations varying track gauge, lateral contact point position and friction coefficient showed squeal only around 1550 Hz and for $\mu_0 = 0.6$. The simulation with track gauge 1447 mm, $\mu_0 = 0.6$, and $Y_w^{(I)} = 13$ mm (the nominal contact point position on the wheel tread for the outer wheel) is analysed in Fig. 13. Similarly to the inner wheel case, the axial vibration amplitude is comparable to the radial one.

5. Comparison with noise and vibration measurements

The results obtained through curve squeal simulations in the time domain are here compared with noise and vibration measurements conducted on site. The curve squeal generated by the tramcar analysed in the previous sections is monitored through trackside microphones and accelerometers mounted on the wheels. The tramcar runs at 10 km/h along a left-hand curve with radius 17.5 m. During the experimental campaign, only one wheel was instrumented at a time, and the results presented here refer to two different

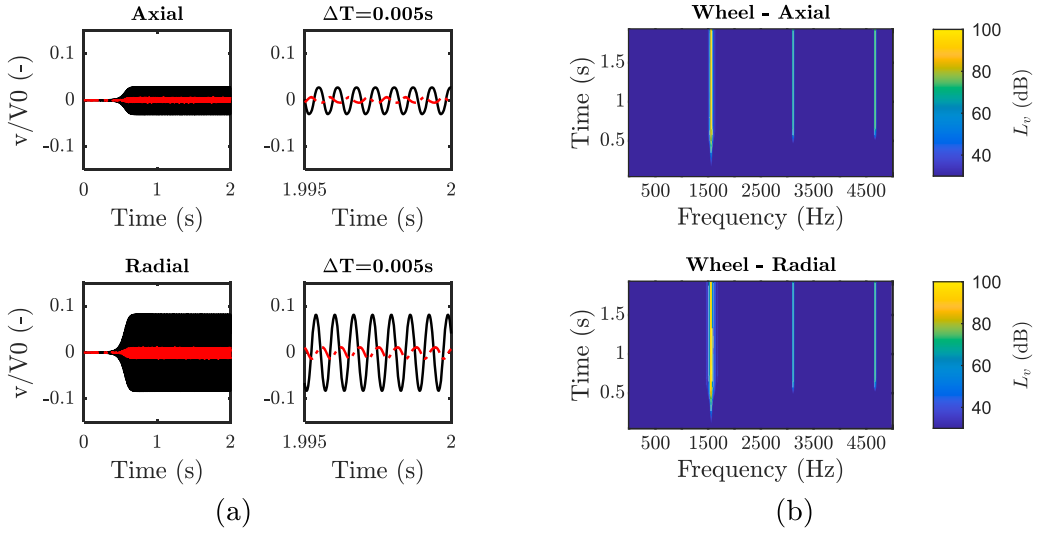

Fig. 11. Curve squeal on the inner wheel in the presence of multiple contact points for $\mu_0 = 0.60$, track gauge 1447 mm and $Y_w^{(I)}$ =21 mm: (a) time evolution of (▬) wheel and (---) rail vibration and (b) spectra of wheel axial and radial fluctuation (dB, re 10^{-6} m/s).

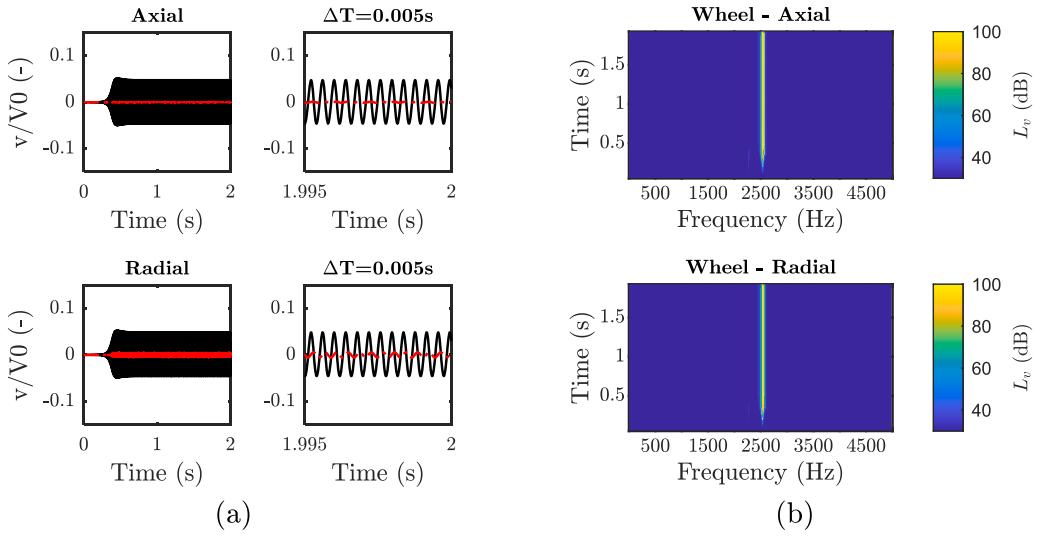

Fig. 12. Curve squeal on the inner wheel in the presence of multiple contact points for $\mu_0 = 0.60$, track gauge 1450 mm and $Y_w^{(I)}$ =15 mm: (a) time evolution of (▬) wheel and (---) rail vibration and (b) spectra of wheel axial and radial fluctuation (dB, re 10^{-6} m/s).

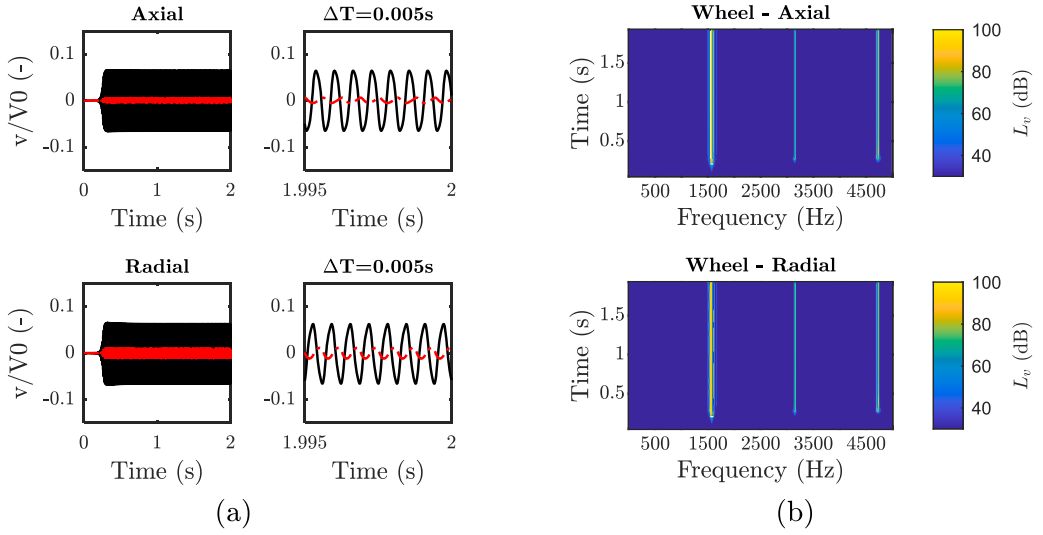

Fig. 13. Curve squeal on the outer wheel in the presence of multiple contact points for $\mu_0 = 0.60$, track gauge 1447 mm and $Y_w^{(I)} = -13$ mm: (a) time evolution of (▬) wheel and (---) rail vibration and (b) spectra of wheel axial and radial fluctuation (dB, re 10^{-6} m/s).

runs. All tests were performed on a dry track.

During the first passage, the vibration of the leading inner wheel of the second bogie is monitored. For the second passage, the instrumented wheel is positioned on the outer side. In both passages, a microphone placed 2.5 m away from the track centreline, on the same side as the instrumented wheel, is employed to measure the noise level generated during the tramcar pass-by. The arrangement of the trackside microphones is illustrated in Fig. 14a. A photograph of the instrumented wheel is shown in Fig. 14b while the position of the accelerometers used to measure the wheel vibration in the axial and radial directions is illustrated in Fig. 14c. The axial and radial accelerometers are mounted at a radial distance of 310 mm from the wheel centre. A telemetry system is used to transmit the signals measured by the accelerometers to an onboard acquisition system. An analog radio signal was acquired by the onboard and trackside measurement systems, in order to synchronize the two sets of measurements.

The vibration analysis of both wheels was carried out over three consecutive passages for each wheel, with all the results shown in Appendix C. Despite some variability and intermittency along the curve, all passes demonstrate a high degree of repeatability in the phenomenon. Therefore, the detailed noise and vibration analysis presented below focuses solely on passage 1 for each wheel. Most of the noise emission (see Fig. 15) is concentrated around 1550 Hz for both the inner and the outer side of the vehicle. The spectrogram highlights that the noise is not completely tonal, but it is characterized by a spread around 1500 Hz. A similar frequency spread is also

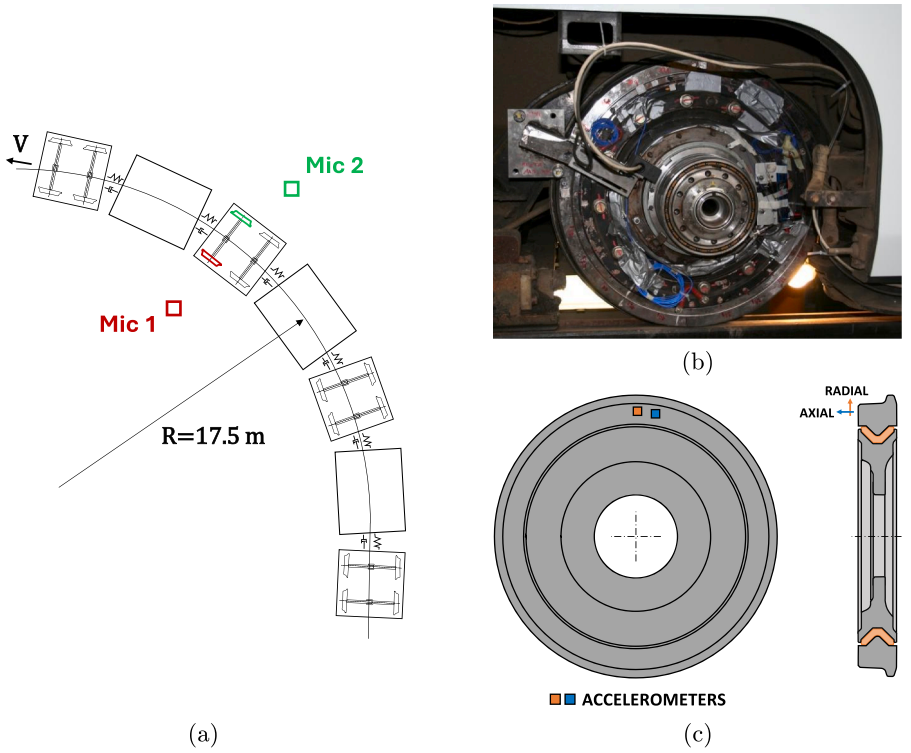

Fig. 14. Experimental setup: (a) trackside microphones, (b) photograph of the instrumented wheel and (c) location of the accelerometers mounted on the wheel.

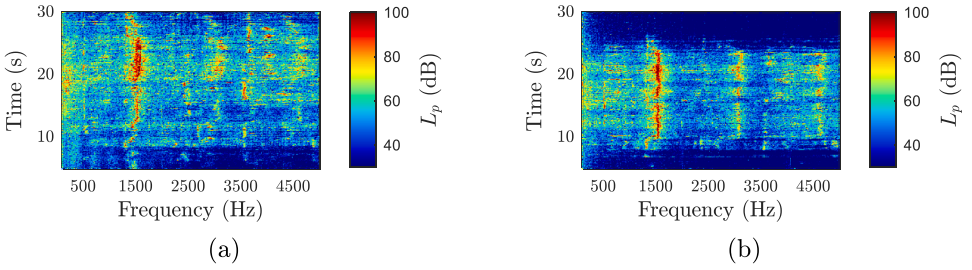

Fig. 15. Spectrograms of the Sound Pressure Level measured by trackside microphone (d = 2.5 m): (a) inner side and (b) outer side (dB, re $2 \cdot 10^{-5}$ Pa).

found in [5,16]. This is attributed to the presence of more than one wheel vibration mode involved in the unstable mechanism. The results presented in [16] suggest that the frequency spread is found only in the presence of a second contact point between the leading inner wheel of the bogie and the grooved head.

As obtained in case of multiple contact points on the inner leading wheel (see Section 4.2), slight variations in contact conditions can alter the squealing frequency. This may lead to variable and intermittent behaviour of the phenomenon along the curve. Although the main cause of this behaviour is not fully understood, it is commonly found in the literature that the contact between the wheel flange and the rail produces a broadband noise referred to as "flange noise" [1,52]. This provides a possible further explanation for the observed frequency spread, which could result from the presence of a "flange-type" contact, at least on the outer wheel or in cases involving flange back contacts, exciting a wider frequency range.

The spectrograms of the wheel acceleration in the axial and radial directions are shown in Fig. 16. They have a frequency content similar to that recorded by the trackside microphone. Significant vibration levels close to 1550 Hz are observed in both axial and radial directions. The vibration level in the radial direction is comparable or higher with respect to the axial one. As also observed in Section 4.3, this is attributed to the characteristics of the wheel modes involved in the squealing event, which are the axial and radial wheel modes with 3 ND. They are both characterized by significant axial and radial components, as also visible in the wheel mobility diagram (see Appendix B). As reported in [5], this favours mode-coupling mechanisms.

The spectrograms of the vibration levels also reveal a short time window in which a tonal contribution close to 550 Hz arises in

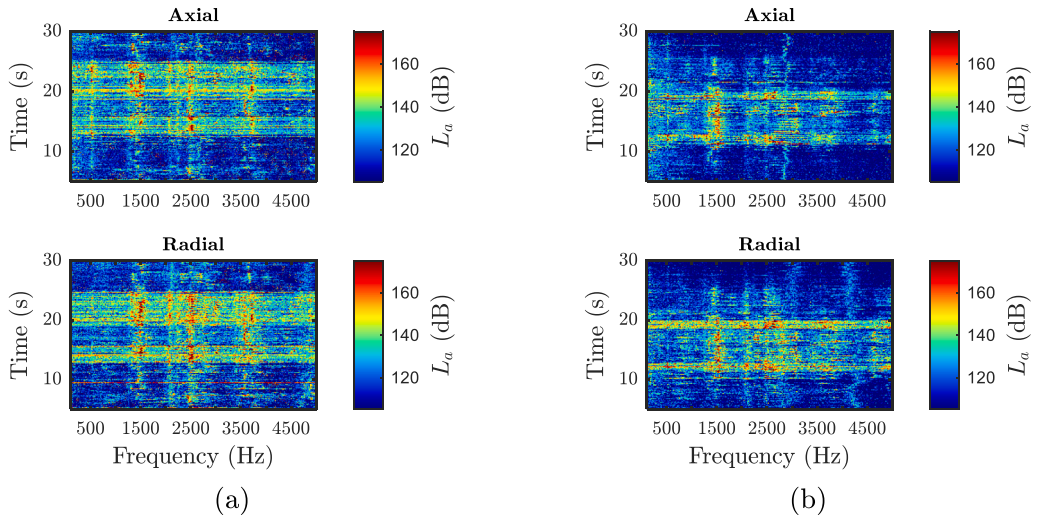

Fig. 16. Spectrograms of the wheel acceleration levels in axial and radial direction: (a) inner wheel and (b) outer wheel (dB, re 10^{-6} m/s^2).

proximity to curve entrance and curve exit. This contribution is more marked on the spectrograms related to the inner wheel (see Fig. 16). Another tonal contribution in the inner wheel vibration is found close to 2500 Hz (see Fig. 16a around 12 s). Again, these contributions are confined in very short time windows during the curve entrance and the curve exit. The same contribution can also be found in the microphone spectrograms, although it is less evident. These two frequencies are very close to the natural frequencies of the wheel axial modes with 2 ND and 4 ND. It should be noted that the noise generated at curve entrance and/or at curve exit and measured by the microphone placed in the middle of the curve is attenuated compared to the noise generated in proximity to the measurement section, on account of the distance between the source and the receiver. This may be the reason why, despite a significant vibration level being measured at the curve entrance and exit by the accelerometers mounted on the wheel, the noise level at the specific frequency recorded in the same time window is lower or less evident as in the acceleration spectrograms. As the transition of each bogie into the curve is not instantaneous, the wheels are subjected to a transient during which they move from a straight track to the steady-state curving conditions. During this transient, the wheel/rail contact condition may vary significantly. Both the inner and

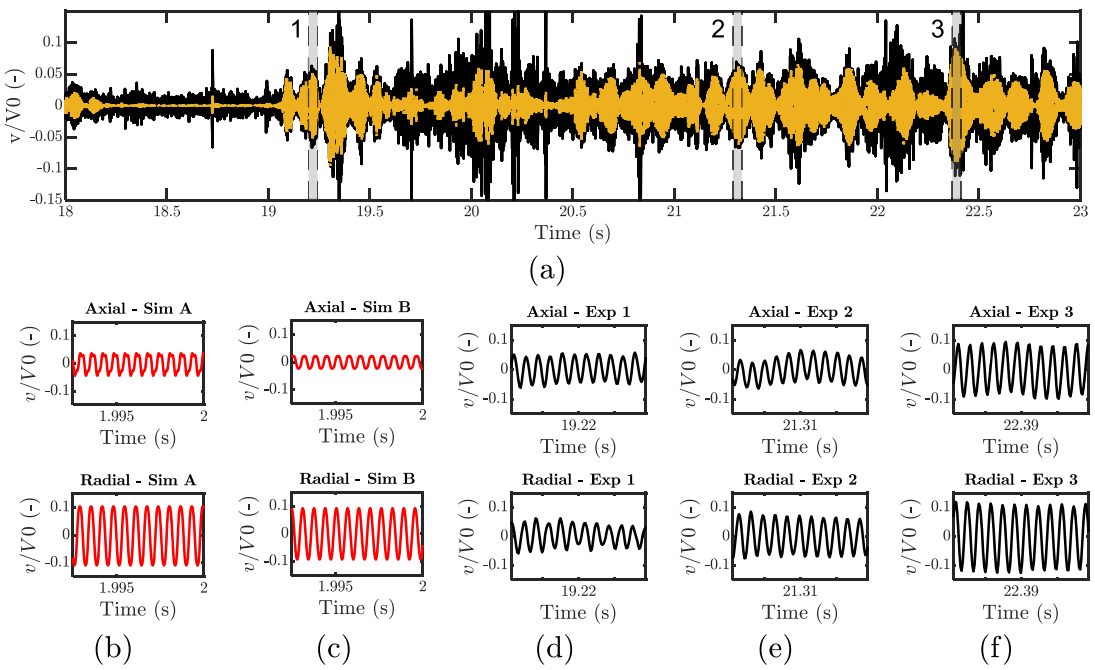

Fig. 17. Comparison between measurements and simulations (track gauge 1447 mm, μ_0=0.6): (a) identification of the limit cycles, (b) simulation with $Y_w^{(I)}$=10 mm, (c) simulation with $Y_w^{(I)}$=20 mm and (d-f) experimental data.

the outer leading wheel start by being centred with respect to the track, with a zero angle of attack between them. When the leading axle is approaching the curve, the angle of attack between the wheels and the rail increases until reaching the steady-state values. Due to the relative lateral displacement between the wheels and the track, the position of the contact point on the wheel also gradually changes. Additionally, the wheel/rail contact forces evolve over time and the load distribution across the different wheels changes during entry into the curve. Thus, different squealing behaviour may be related to transient phenomena associated with wheel/rail contact conditions that are different from the steady-state ones. This is consistent with numerical simulations, where squeal is predicted close to 535 Hz, 1550 Hz and 2500 Hz. Moreover, the presence of track irregularities along the curve may alter the load distribution on the flange and on the flange back contacts. Similarly, the friction coefficient may vary locally in different portions of the track. This may be another reason why the same wheel is excited at different frequencies during the curve negotiation.

Vibration measurements are compared with the results of the numerical simulations. Two main time windows are analysed for the inner wheel, which is unstable at frequencies close to 1500 Hz after 19 s and close to 2500 Hz around 12 s. The amplitude of the axial and radial vibration of the wheel during these squealing events is compared with the results obtained in the simulations with a track gauge of 1447 mm and 1450 mm and μ_0=0.6. This adhesion condition is the only one in which squeal is numerically observed on both the inner and outer wheels, consistent with observations from the test campaign. Since the measurements were carried out on a sunny day with a dry track, this choice of the friction coefficient is considered potentially representative of the adhesion conditions during testing. Given that the accelerometers are installed on a rotating wheel, the comparison between the measured and predicted vibrations can be carried out only over very short time windows. For this reason, only the windows in which the amplitude of the measured vibrations is maximum are used for the numerical-experimental comparison. The experimental vibration velocity is computed by integrating the acceleration signal. A bandpass filter is applied to highlight the wheel vibration at 1500 Hz and at 2500 Hz. Data are collected into pairs of adjacent one-third octave bands, considering the signal contribution in the frequency ranges 1130–1760 Hz and 1760–2825 Hz. This procedure is employed solely to identify the short time windows for the experimental comparison. Once these windows are determined, the raw data (black line in Fig. 17a) are used for comparison with the numerical results. Significant wear was observed on the grooved head suggesting that a flange back contact is activated most of the time during the curve negotiation. Therefore, a first analysis compares the results of the simulation with two contact points for a track gauge of 1447 mm with the tonal wheel vibration measured near 1550 Hz. Fig. 17a shows the time history of the axial vibration velocity when the wheel is squealing at 1550 Hz. The signal contribution in the 1130–1760 Hz frequency range is highlighted, along with the three short time windows used for comparison with the numerical results (Fig. 17b). Data are normalized by vehicle speed. The comparison is reported in Fig. 17, where two numerical simulations ($Y_w^{(I)}$=10 mm and $Y_w^{(I)}$=20 mm) are compared with three experimental windows. Although this type of analysis can only be limited to qualitative observations, a satisfactory agreement is observed between the simulations and the experimental data. The squealing frequency closely matches that observed in the wheel vibration spectrograms, and the vibration amplitude is consistent with the measured values yet remains subject to some variability.

The same analysis is carried out for squeal at 2500 Hz (now only the signal contribution in the frequency range 1760–2825 Hz is

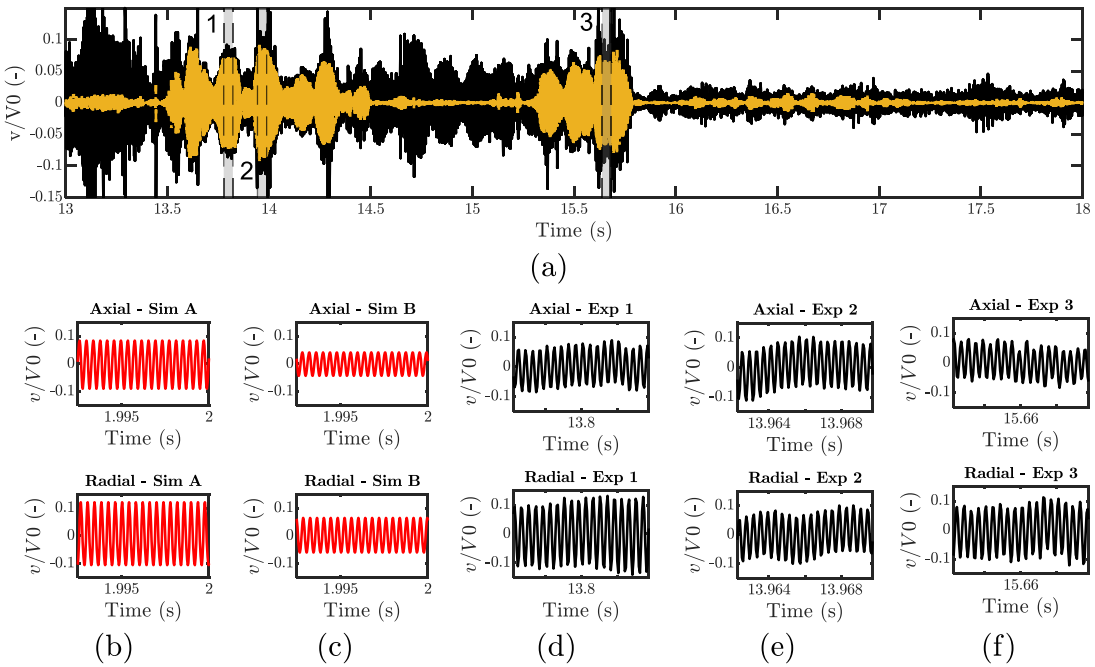

Fig. 18. Comparison between measurements and simulations (track gauge 1450 mm, μ_0=0.6): (a) identification of the limit cycles, (b) simulation with $Y_w^{(I)}$=5 mm, (c) simulation with $Y_w^{(I)}$=15 mm and (d-f) experimental data.

highlighted). The simulation with a track gauge of 1450 mm is here employed for comparison and the results are shown in Fig. 18. Similar wheel vibration amplitude in the axial and radial directions is observed when the experimental limit cycle reaches its maximum value.

Similarly to the inner wheel case, measurements are compared with squeal simulations carried out considering the outer leading wheel. The previous analyses were made under the assumption of multiple contact points between the wheel and the rail, adopting the results from the simulations with track gauge of 1447 mm and 1450 mm. Only the results with a track gauge of 1447 mm and μ_0=0.6 are here used for the comparison with measurements because similar results are obtained with other track gauges. Results are shown in Fig. 19. Also, for the outer wheel, a good agreement between the measurements and the simulation results is found for the wheel vibration in the axial and radial directions.

The time histories shown above enable a qualitative comparison between the simulation results and the measured data. A full validation of the squeal model against on-site data is currently unattainable due to numerous uncertainties such as exact contact positions, contact forces, variability along the curve, and environmental factors including temperature and humidity. Nevertheless, the objective is to ensure that the model predictions of squeal frequencies and vibration amplitudes remain consistent with the measurements obtained on site. A qualitative comparison is provided overall, while an attempt is also made to quantify the difference between model and measurements for selected short time windows (see Fig. 20). These windows are not fully representative of the entire problem but reflect what can reasonably be obtained from the available on-site data. Although axial vibration measurements confirm that a rough, yet reasonable estimation of the wheel vibration amplitude can be obtained using $v_{max} = \psi \cdot V_0$ as reported in [1, 9,19] (where ψ is the angle of attack and V_0 is the rolling speed), the simulations provide further insights and a more detailed description of the phenomenon, while also enabling the estimation of wheel vibrations in the radial direction. For example, variability in vibration levels due to the shift in the contact point position is detected. This is more pronounced on the inner wheel (up to 5 dB), while it remains limited on the outer wheel (below 2 dB). This result demonstrates that contact conditions play a key role not only in the onset of the phenomenon or in determining the squealing frequency, but also in defining the limit-cycle vibration levels. The variability detected in measured vibration levels may instead be attributed to several factors, since each time window represents a snapshot of a different point along the curve and may therefore reflect significant variations in wheel/rail contact conditions (e.g. wheel/rail roughness, friction coefficient, rail profile wear, and track misalignment). Although the variability of the results is in some cases rather pronounced, in the three scenarios considered several pairs of numerical and experimental levels differ by less than 2–3 dB in both axial and radial vibration levels. This agreement can be considered satisfactory given the complexity of the wheel/rail contact conditions and the simplifications introduced in the wheel/rail interaction model.

The numerical simulations do not account for wheel/rail irregularities and roughness, which would introduce an additional broadband excitation in the system, with an amplitude that decreases with frequency (as the PSD of the wheel/rail roughness decreases with the wavelength) [1,42]. Therefore, this experimental comparison should not be regarded as a detailed or comprehensive validation of the wheel/rail interaction model, which would require measurements in a controlled environment and a precise knowledge of the wheel/rail contact conditions during squeal events. Nevertheless, the analysis represents the first attempt at verification using

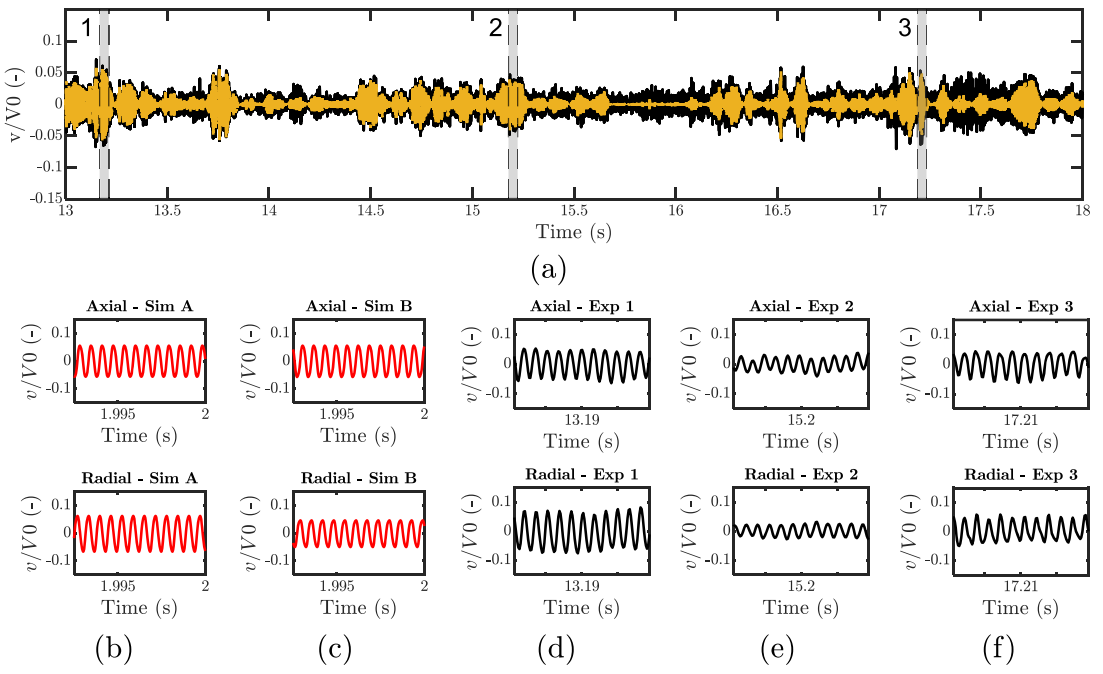

Fig. 19. Comparison between measurements and simulations (track gauge 1447 mm, μ_0=0.6): (a) identification of the limit cycles, (b) simulation with $Y_w^{(I)}$=−5 mm, (c) simulation with $Y_w^{(I)}$=−15 mm and (d-f) experimental data.

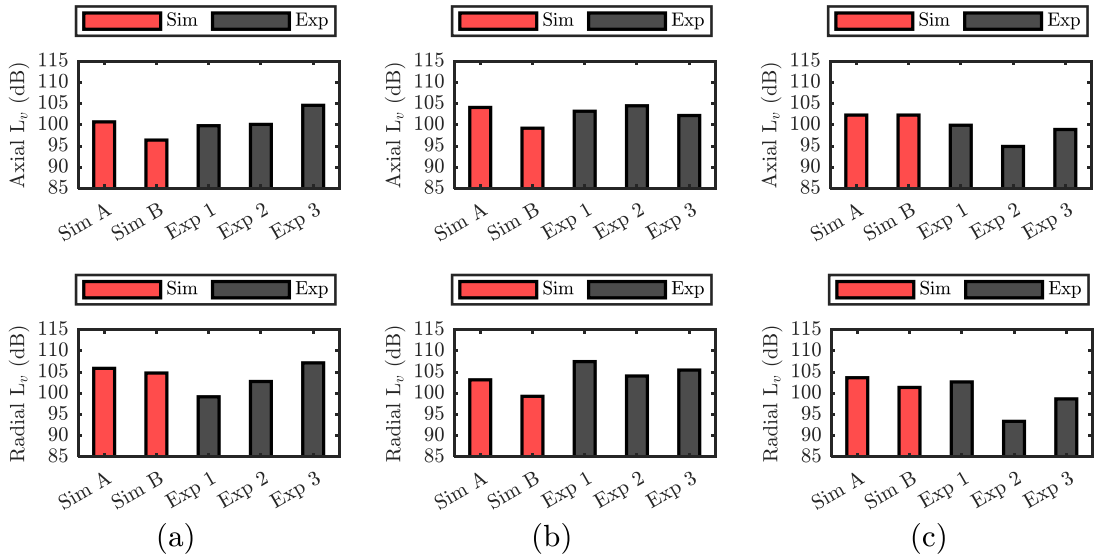

Fig. 20. Overview of the vibration levels in axial and radial directions (dB, re 10^{-6} m/s) obtained in simulations (■) and measurements (■): (a) inner wheel, track gauge 1447 mm, (b) inner wheel, track gauge 1450 mm and (c) outer wheel, track gauge 1447 mm.

full-scale on-track measurements, demonstrating that this numerical approach can satisfactorily estimate squeal frequencies and vibration amplitudes even in the presence of multiple wheel/rail contact points. Moreover, the results indicate that, for curve squeal, a parametric approach accounting for a wide range of variability in the contact parameters is preferable, not only for predicting squeal frequencies but also for estimating vibration and noise levels.

6. Conclusions

A methodology for curve squeal prediction in frequency and time domain is introduced, which accounts for the possible simultaneous presence of multiple contact points between the wheel and the rail. The previous formulations of wheel/rail interaction in the presence of multiple contact points did not allow performing CEA to track the eigenvalue evolution as a function of specific wheel/rail contact parameters. The state-space formulation proposed in this article overcomes this limitation. Furthermore, the simplified approach previously developed by the authors has been extended and thoroughly revised to include the longitudinal dynamics, the rail dynamics, and the presence of a second contact point in the time domain simulations. The contact force formulation has also been refined by incorporating an unsteady tangential contact model based on Kalker's variational theory. This allows capturing potential unsteady phenomena occurring in high-frequency wheel/rail contact, in line with previous studies but now also including the effect of a slip-dependent friction coefficient. The model reproduces the typical contact conditions that can be found on the leading wheelset of a bogie running in sharp curves. It is employed to analyse the squeal generated by a modern articulated tramcar. The dynamic models of the wheel and the rail are tuned using experimental tests. In particular, the modal model of the wheel is calibrated against Experimental Modal Analysis (EMA) on the resilient wheel mounted on the tramcar while the rail dynamics is included by fitting the Frequency Response Functions (FRFs) obtained through an impact test on a tramway track with grooved rails.

Three main situations are investigated through frequency and time-domain simulations. In the first situation, simulations are carried out by considering a single contact point between the wheel and the rail, where there is a contact between the wheel tread and the top of the rail. This is the typical wheel/rail contact condition experienced by the leading inner wheel of a bogie negotiating a curve. Squeal is observed for a friction coefficient higher than 0.3 in proximity to the axial wheel mode with 2 ND.

In the second situation, the effect of the contact between the back of the wheel flange and the grooved head is investigated. The second contact point is progressively activated by varying the track gauge. This allows for a parametric investigation into the effect of the load on the flange back. The impact of the contact point position on the wheel tread is also investigated. The analysis is repeated under different adhesion conditions, showing that curve squeal is always favoured by a high friction coefficient. In this contact condition, squeal is observed for friction coefficients starting from $\mu_0 = 0.45$. Unlike the single contact point case, in the presence of two contact points squeal is promoted by the dynamic coupling between lateral and vertical dynamics and therefore develops even in the absence of falling friction. Furthermore, the presence of the second contact point alters the frequency involved in the squeal event compared with the single contact point case. Similarly, a variation in the load on the flange back or in the lateral contact point position on the wheel tread is found to activate different wheel vibration modes. These results show that a small variation in the wear conditions or in the relative position between the wheel and the rail may generate squeal at different frequencies, making the curve squeal phenomenon highly unpredictable.

In the third situation, numerical simulations are carried out to study curve squeal of the outer leading wheel, which is in contact with the rail head and the rail gauge face. Simulations reveal that also the outer wheel can squeal. In this case, squeal is observed only

for a friction coefficient of $\mu_0 = 0.6$, and it still develops even when the slip-dependent friction coefficient is neglected.

Finally, the model is verified against experimental measurements. In particular, the time domain curve squeal simulations are compared with full-scale on-track measurements using accelerometers mounted on the squealing wheels. Measurements are carried out during the negotiation of a curve with radius of 17.5 m. Pass-by noise levels and the vibration of the leading inner and outer wheels of the second bogie in the axial and radial directions were measured. The model is found to predict the occurrence of curve squeal at the same frequencies observed during pass-by tests. Additionally, good agreement between the amplitude of the wheel vibration measured and that estimated by the numerical model is obtained.

CRediT authorship contribution statement

Federico Castellini: Writing – review & editing, Writing – original draft, Visualization, Validation, Software, Methodology, Investigation, Formal analysis, Data curation, Conceptualization. **Giacomo Squicciarini:** Writing – review & editing, Supervision, Resources, Project administration, Methodology, Investigation, Formal analysis, Data curation, Conceptualization. **David Thompson:** Writing – review & editing, Supervision, Methodology, Investigation, Formal analysis, Conceptualization. **Egidio Di Gialleonardo:** Writing – review & editing, Supervision, Resources, Project administration, Methodology, Investigation, Formal analysis, Data curation, Conceptualization. **Roberto Corradi:** Supervision, Project administration, Funding acquisition.

Declaration of competing interest

The authors declare that they have no known competing financial interests or personal relationships that could have appeared to influence the work reported in this paper.

Appendix A. Parameters of the vehicle dynamics simulations

The steady-state curving parameters of the leading inner and outer wheels obtained from the vehicle dynamics simulations in case of μ_0=0.45 and μ_0=0.60 are reported in Table A1 and Table A2.

Table A1
Results of vehicle dynamics simulations ($\mu_0 = 0.45$).

Track gauge: 1445 mm						**Track gauge: 1446 mm**					
		Inner		**Outer**				**Inner**		**Outer**	
		CP I	CP II	CP I	CP II			CP I	CP II	CP I	CP II
Normal load	F_3 (kN)	25.9	-	8.4	23.6	Normal load	F_3 (kN)	25.8	-	8.4	23.7
Angle of attack	ψ (deg)	2.9	-	2.9	2.9	Angle of attack	ψ (deg)	2.9	-	2.9	2.9
Long. Creepage	γ_1 $(-)$	0.00	-	0.02	-0.00	Long. Creepage	γ_1 $(-)$	0.00	-	0.02	0.00
Transverse Creepage	γ_2 $(-)$	0.05	-	0.05	0.16	Transverse Creepage	γ_2 $(-)$	0.05	-	0.05	0.16
Spin Creepage	$\gamma_6(1/m)$	-0.07	-	0.21	2.91	Spin Creepage	$\gamma_6(1/m)$	-0.06	-	0.21	2.91
Contact Angle	θ (deg)	2.5	-	-2.8	-70.1	Contact Angle	θ (deg)	2.5	-	-2.8	-70.1
Lateral CP position	Y_w (mm)	22	-	-13	19	Lateral CP position	Y_w (mm)	22	-	-13	19
Track gauge: 1447 mm						**Track gauge: 1448 mm**					
		Inner		**Outer**				**Inner**		**Outer**	
		CP I	CP II	CP I	CP II			CP I	CP II	CP I	CP II
Normal load	F_3 (kN)	19.4	7.4	15.0	15.4	Normal load	F_3 (kN)	18.6	8.2	15.3	14.8
Angle of attack	ψ (deg)	2.9	2.9	2.9	2.9	Angle of attack	ψ (deg)	2.9	2.9	2.9	2.9
Long. Creepage	γ_1 $(-)$	0.00	-0.02	0.01	-0.02	Long. Creepage	γ_1 $(-)$	0.00	-0.02	0.01	-0.02
Transverse Creepage	γ_2 $(-)$	0.05	0.13	0.05	0.16	Transverse Creepage	γ_2 $(-)$	0.05	0.12	0.05	0.16
Spin Creepage	γ_6 $(1/m)$	-0.07	2.74	0.21	2.95	Spin Creepage	γ_6 $(1/m)$	-0.08	2.68	0.21	2.95
Contact Angle	θ (deg)	2.6	-70.8	-2.8	-70.1	Contact Angle	θ (deg)	2.7	-67.3	-2.8	-70.1
Lateral CP position	Y_w (mm)	21	-42	-13	19	Lateral CP position	Y_w (mm)	21	-42	-12	19
Track gauge: 1449 mm						**Track gauge: 1450 mm**					
		Inner		**Outer**				**Inner**		**Outer**	
		CP I	CP II	CP I	CP II			CP I	CP II	CP I	CP II
Normal load	F_3 (kN)	16.3	10.9	17.4	12.0	Normal load	F_3 (kN)	9.4	20.7	25.5	1.0
Angle of attack	ψ (deg)	2.9	2.9	2.9	2.9	Angle of attack	ψ (deg)	2.9	2.9	2.9	2.9
Long. Creepage	γ_1 $(-)$	0.00	-0.02	0.00	-0.02	Long. Creepage	γ_1 $(-)$	0.02	-0.00	0.00	-0.02
Transverse Creepage	γ_2 $(-)$	0.05	0.13	0.05	0.16	Transverse Creepage	γ_2 $(-)$	0.05	0.13	0.05	0.16
Spin Creepage	$\gamma_6(1/m)$	-0.08	2.67	0.21	2.96	Spin Creepage	$\gamma_6(1/m)$	-0.08	2.69	0.21	2.98
Contact Angle	θ (deg)	2.8	-67.3	-2.8	-70.1	Contact Angle	θ (deg)	2.8	-70.7	-2.8	-70.1
Lateral CP position	Y_w (mm)	20	-42	-13	19	Lateral CP position	Y_w (mm)	20	-42	-13	19

Table A2
Results of vehicle dynamics simulations ($\mu_0 = 0.60$).

Track gauge: 1445 mm						**Track gauge: 1446 mm**					
		Inner		**Outer**				**Inner**		**Outer**	
		CP I	CP II	CP I	CP II			CP I	CP II	CP I	CP II
Normal load	F_3 (kN)	25.9	-	1.6	27.7	Normal load	F_3 (kN)	23.3	2.6	4.2	24.7
Angle of attack	ψ (deg)	2.9	-	2.9	2.9	Angle of attack	ψ (deg)	2.9	2.9	2.9	2.9
Long. Creepage	γ_1 (−)	0.00	-	0.04	0.01	Long. Creepage	γ_1 (−)	0.00	-0.03	0.03	0.00
Transverse Creepage	γ_2 (−)	0.05	-	0.05	0.16	Transverse Creepage	γ_2 (−)	0.05	0.12	0.05	0.16
Spin Creepage	$\gamma_6(1/m)$	-0.06	-	0.20	2.85	Spin Creepage	$\gamma_6(1/m)$	-0.07	2.67	0.20	2.88
Contact Angle	θ (deg)	2.5	-	-2.8	-70.1	Contact Angle	θ (deg)	2.5	-66.1	-2.8	-70.1
Lateral CP position	Y_w (mm)	22	-	-13	19	Lateral CP position	Y_w (mm)	22	-42	-13	19
Track gauge: 1447 mm						**Track gauge: 1448 mm**					
		Inner		**Outer**				**Inner**		**Outer**	
		CP I	CP II	CP I	CP II			CP I	CP II	CP I	CP II
Normal load	F_3 (kN)	16.8	9.1	11.2	17.2	Normal load	F_3 (kN)	15.6	10.2	11.9	16.4
Angle of attack	ψ (deg)	2.9	2.9	2.9	2.9	Angle of attack	ψ (deg)	2.9	2.9	2.9	2.9
Long. Creepage	γ_1 (−)	0.00	-0.02	0.01	-0.01	Long. Creepage	γ_1 (−)	0.00	-0.02	0.01	-0.01
Transverse Creepage	γ_2 (−)	0.05	0.13	0.05	0.16	Transverse Creepage	γ_2 (−)	0.05	0.13	0.05	0.16
Spin Creepage	$\gamma_6(1/m)$	-0.07	2.74	0.21	2.93	Spin Creepage	$\gamma_6(1/m)$	-0.07	2.67	0.21	2.94
Contact Angle	θ (deg)	2.6	-70.9	-2.8	-70.1	Contact Angle	θ (deg)	2.7	-67.0	-2.8	-70.1
Lateral CP position	Y_w (mm)	21	-42	-13	19	Lateral CP position	Y_w (mm)	20	-42	-11	19
Track gauge: 1449 mm						**Track gauge: 1450 mm**					
		Inner		**Outer**				**Inner**		**Outer**	
		CP I	CP II	CP I	CP II			CP I	CP II	CP I	CP II
Normal load	F_3 (kN)	13.2	12.5	14.0	13.9	Normal load	F_3 (kN)	6.3	20.6	21.9	4.6
Angle of attack	ψ (deg)	2.9	2.9	2.9	2.9	Angle of attack	ψ (deg)	2.9	2.9	2.9	2.9
Long. Creepage	γ_1 (−)	0.01	-0.02	0.01	-0.01	Long. Creepage	γ_1 (−)	0.02	-0.00	0.00	-0.02
Transverse Creepage	γ_2 (−)	0.05	0.13	0.05	0.16	Transverse Creepage	γ_2 (−)	0.05	0.13	0.05	0.16
Spin Creepage	$\gamma_6(1/m)$	-0.08	2.65	0.21	2.95	Spin Creepage	$\gamma_6(1/m)$	-0.08	2.68	0.21	2.97
Contact Angle	θ (deg)	2.8	-66.9	-2.8	-70.1	Contact Angle	θ (deg)	2.8	-70.7	-2.8	-70.1
Lateral CP position	Y_w (mm)	20	-42	-13	19	Lateral CP position	Y_w (mm)	20	-42	-13	19

Appendix B. Wheel and rail dynamics

Modal models are used to reproduce the dynamic behaviour of the wheel and the rail up to 5 kHz, which is typically the frequency range of interest for studying curve squeal phenomena [1] and corresponds to the frequency range observed in the measurements. A FE model of the resilient wheel mounted on the tramcar has been developed to include the wheel dynamics at contact points. The modal model of the wheel consists of the natural frequencies and modal damping ratios measured experimentally along with the mode shapes obtained from the FE model [16]. A total number of 67 modes are considered. A modeshape matrix for each contact point is generated. The longitudinal, lateral and vertical wheel FRFs are reported in Fig. B.1. The lateral and vertical wheel FRFs are compared with the measured ones. The resonance peaks corresponding to the wheel axial and radial vibration modes with 2,3 and 4 Nodal Diameters (ND) are also highlighted (more details of the wheel vibration modes and the modal damping ratios are provided in [16]). No measured FRFs are available for the longitudinal dynamics.

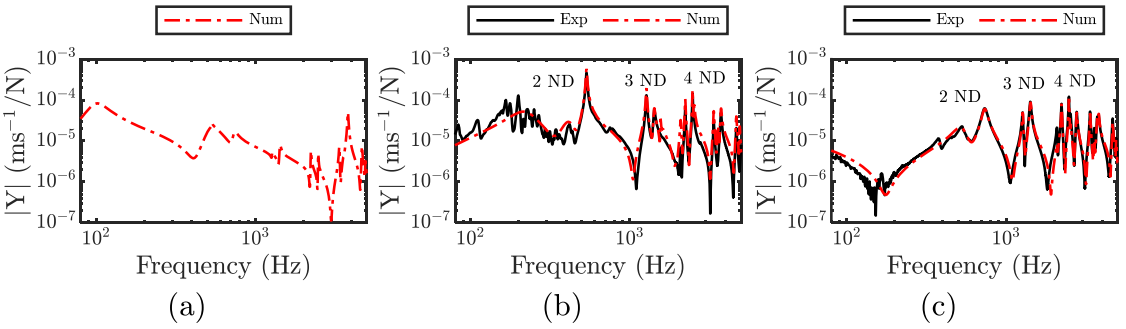

Fig. B.1. Wheel mobility: (a) longitudinal, (b) lateral and (c) vertical [16,31,35].

The rail dynamics is included through an equivalent modal model. A least-squares minimisation is used to estimate the modal parameters of the rail by comparing the FRFs generated by the equivalent modal model with the ones obtained from measurements and

numerical simulations. A set of three equivalent modes is used for fitting the FRFs, which ensures a good match with the track average mobility up to 5 kHz (see Fig. B.2. The rail dynamics in longitudinal direction is introduced calibrating the equivalent modal model with a rod analytical model on a layer of damped springs. According to [1], the parameter of the model employed to calculate the rail mobility in longitudinal directions are estimated by using the foundation stiffness parameter obtained to fit the rail lateral frequency response functions with an infinite beam model on a single viscoelastic foundation (the parameters are reported in [35]). This article assumes identical rail mobility at the different contact points. As discussed in Section 3, although cross-terms are not explicitly included, direct coupling between the two contact points is considered: a vertical force at one point induces vertical vibration at the other, and vice versa. This applies to all directions. Lateral-vertical coupling is still accounted for through the contact forces, as the normal and tangential components at each contact point are always reprojected into the x, y, and z reference frame.

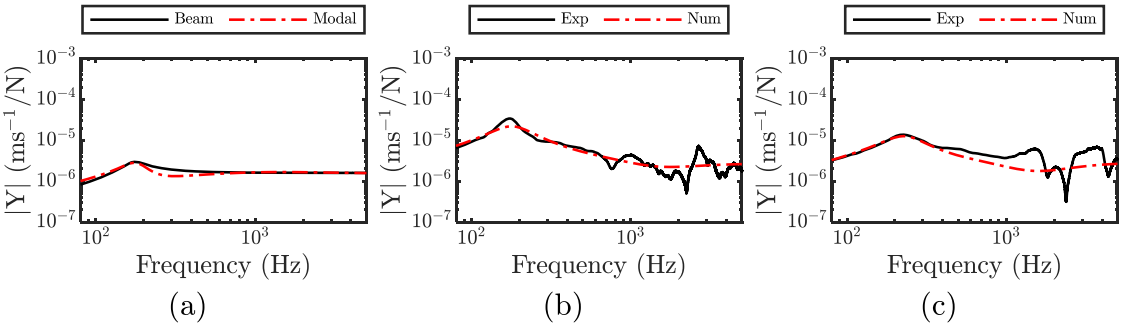

Fig. B.2. Rail mobility: (a) longitudinal, (b) lateral and (c) vertical.

Appendix C. Noise and vibration measurements

This appendix presents the results of vibration and noise measurements performed during consecutive passes of the analysed vehicle. The spectrograms of the noise measured by the track-side microphone (facing the inner and outer wheel) are reported, along with the spectrograms of the vibrations of the inner and outer leading wheels in the axial and radial directions for each pass (see Fig. C.1 and Fig. C.2).

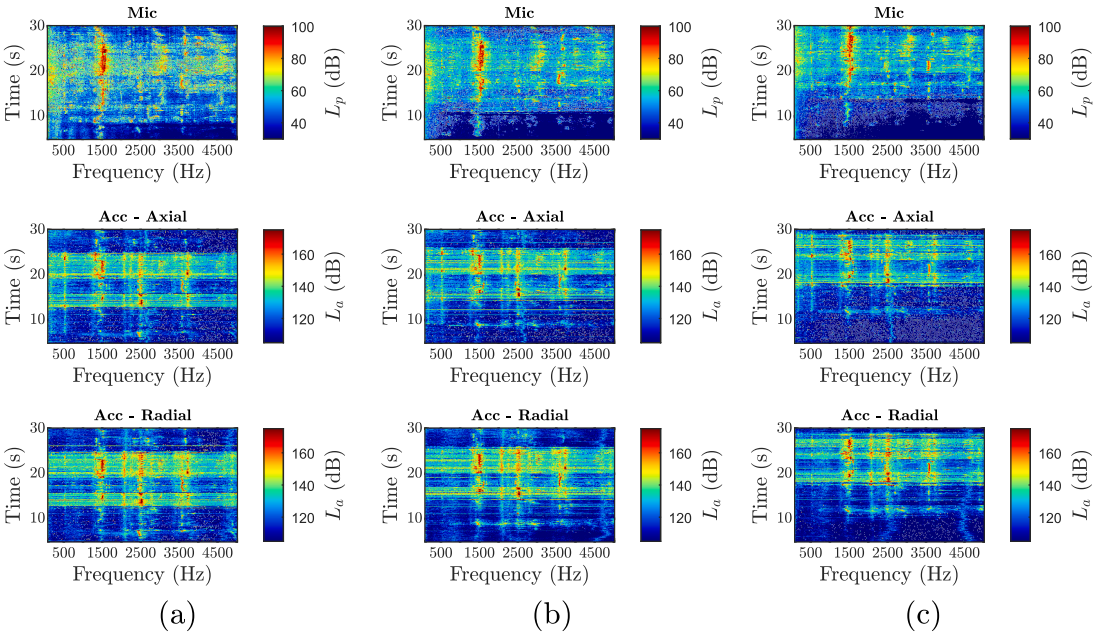

Fig. C.1. Spectrograms of the sound pressure levels (dB, re $2{\cdot}10^{-5}$ Pa) and of the inner wheel acceleration levels (dB, re 10^{-6} m/s^2): (a) passage 1, (b) passage 2 and (c) passage 3.

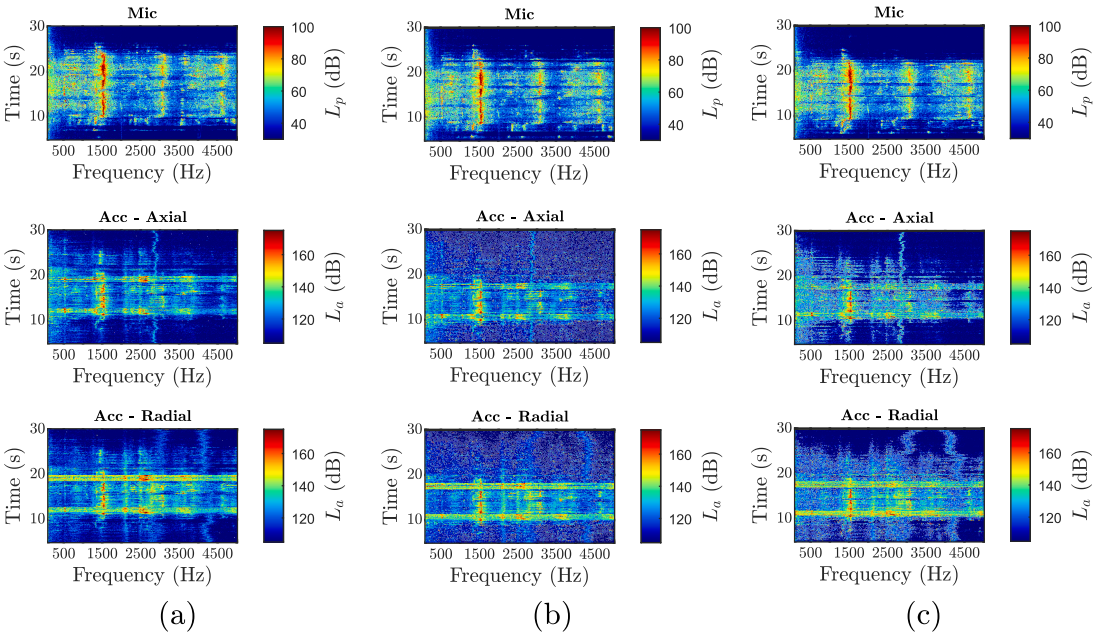

Fig. C.2. Spectrograms of the sound pressure levels (dB, re $2{\cdot}10^{-5}$ Pa) and of the outer wheel acceleration levels (dB, re 10^{-6} m/s^2): (a) passage 1, (b) passage 2 and (c) passage 3.

Data availability

The data that has been used is confidential.

References

[1] D. Thompson, Railway Noise and Vibration: Mechanisms, Modelling and Means of Control, Elsevier, Amsterdam, 2024, https://doi.org/10.1016/C2012-0-07344-9.
[2] M.J. Rudd, Wheel/rail noise-Part II: wheel squeal, J. Sound. Vib. 46 (1976) 381–394, https://doi.org/10.1016/0022-460X(76)90862-2.
[3] N. Hoffmann, M. Fischer, R. Allgaier, L. Gaul, A minimal model for studying properties of the mode-coupling type instability in friction induced oscillations, Mech. Res. Commun. 29 (2002) 197–205, https://doi.org/10.1016/S0093-6413(02)00254-9.
[4] P.A. Meehan, Prediction of wheel squeal noise under mode coupling, J. Sound. Vib. 465 (2020), https://doi.org/10.1016/J.JSV.2019.115025.
[5] B. Ding, G. Squicciarini, D. Thompson, R. Corradi, An assessment of mode-coupling and falling-friction mechanisms in railway curve squeal through a simplified approach, J. Sound. Vib. 423 (2018) 126–140, https://doi.org/10.1016/J.JSV.2018.02.048.
[6] S. Liu, U. De Silva, D. Chen, A.C. Leslie, P.A. Meehan, Investigation of wheel squeal noise under mode coupling using two-disk testrig experiments, Wear. 530–531 (2023) 205035, https://doi.org/10.1016/J.WEAR.2023.205035.
[7] B. Ding, G. Squicciarini, D. Thompson, Effect of rail dynamics on curve squeal under constant friction conditions, J. Sound. Vib. 442 (2019) 183–199, https://doi.org/10.1016/J.JSV.2018.10.027.
[8] V.V. Lai, O. Chiello, J.F. Brunel, P. Dufrénoy, The critical effect of rail vertical phase response in railway curve squeal generation, Int. J. Mech. Sci. 167 (2020), https://doi.org/10.1016/J.IJMECSCI.2019.105281.
[9] D.J. Thompson, G. Squicciarini, B. Ding, L. Baeza, A state-of-the-art review of curve squeal noise: phenomena, mechanisms, modelling and mitigation, Notes Numer. Fluid Mech. Multidiscip. Des. 139 (2018) 3–41, https://doi.org/10.1007/978-3-319-73411-8_1.
[10] M.A. Heckl, I.D. Abrahams, Curve squeal of train wheels, Part 1: mathematical model for its generation, J. Sound. Vib. 229 (2000) 669–693, https://doi.org/10.1006/jsvi.1999.2510.
[11] M.A. Heckl, Curve squeal of train wheels, Part 2: which wheel modes are prone to squeal? J. Sound. Vib. 229 (2000) 695–707, https://doi.org/10.1006/jsvi.1999.2511.
[12] F.G. De Beer, M.H.A. Janssens, P.P. Kooijman, Squeal noise of rail-bound vehicles influenced by lateral contact position, J. Sound. Vib. 267 (2003) 497–507, https://doi.org/10.1016/S0022-460X(03)00710-7.
[13] Z. Huang, Theoretical Modelling of Railway Curve squeal, PhD Thesis, University of Southampton, 2007.
[14] S.S. Hsu, Z. Huang, S.D. Iwnicki, D.J. Thompson, C.J.C. Jones, G. Xie, P.D. Allen, Experimental and theoretical investigation of railway wheel squeal, Proc. Inst. Mech. Eng. F. J. Rail. Rapid. Transit. 221 (2007) 59–73, https://doi.org/10.1243/0954409JRRT85.
[15] G. Squicciarini, S. Usberti, D.J. Thompson, R. Corradi, A. Barbera, Curve Squeal in the Presence of Two Wheel/Rail Contact Points. Notes On Numerical Fluid Mechanics and Multidisciplinary Design, Springer, 2015, pp. 603–610, https://doi.org/10.1007/978-3-662-44832-8_71.
[16] F. Castellini, L. Faccini, E. Di Gialleonardo, S. Alfi, R. Corradi, G. Squicciarini, D. Thompson, Curve squeal in sharp curves: effect of multiple wheel/rail contact points, Appl. Acoust. 218 (2024), https://doi.org/10.1016/J.APACOUST.2024.109862.
[17] F. Castellini, L. Faccini, E. Di Gialleonardo, S. Alfi, R. Corradi, G. Squicciarini, Predictive Modelling of Curve Squeal Occurrence in Tramways: Influence of Wheel/Rail Double Contact Points, in: Noise and Vibration Mitigation For Rail Transportation Systems, Springer, 2024, pp. 501–509.
[18] B. Ding, The Mechanism of Railway Curve Squeal, University of Southampton, 2018.
[19] O. Chiello, J.B. Ayasse, N. Vincent, J.R. Koch, Curve squeal of urban rolling stock-Part 3: theoretical model, J. Sound. Vib. 293 (2006) 710–727, https://doi.org/10.1016/j.jsv.2005.12.010.

[20] V.V. Lai, M. Anciant, O. Chiello, J.F. Brunel, P. Dufrénoy, A nonlinear FE model for wheel/rail curve squeal in the time-domain including acoustic predictions, Appl. Acoust. 179 (2021), https://doi.org/10.1016/J.APACOUST.2021.108031.
[21] J. Giner-Navarro, J. Martínez-Casas, F.D. Denia, L. Baeza, Study of railway curve squeal in the time domain using a high-frequency vehicle/track interaction model, J. Sound. Vib. 431 (2018) 177–191, https://doi.org/10.1016/J.JSV.2018.06.004.
[22] A. Pieringer, Time-domain Modelling of High-Frequency Wheel/Rail interaction, PhD Thesis, Chalmers University of Technology, 2011.
[23] A. Pieringer, A numerical investigation of curve squeal in the case of constant wheel/rail friction, J. Sound. Vib. 333 (2014) 4295–4313, https://doi.org/10.1016/J.JSV.2014.04.024.
[24] I. Zenzerovic, W. Kropp, A. Pieringer, Influence of spin creepage and contact angle on curve squeal: a numerical approach, J. Sound. Vib. 419 (2018) 268–280, https://doi.org/10.1016/j.jsv.2018.01.004.
[25] I. Zenzerovic, W. Kropp, A. Pieringer, An engineering time-domain model for curve squeal: tangential point-contact model and Green's functions approach, J. Sound. Vib. 376 (2016) 149–165, https://doi.org/10.1016/J.JSV.2016.04.037.
[26] P.A. Meehan, X. Liu, Modelling and mitigation of wheel squeal noise amplitude, J. Sound. Vib. 413 (2018) 144–158, https://doi.org/10.1016/j.jsv.2017.10.032.
[27] R. Corradi, A. Facchinetti, S. Manzoni, M. Vanali, Effects of track parameters and environmental conditions on tramcar induced squeal noise, in: ISMA2006: International Conference on Noise and Vibration Engineering, 2006, pp. 3745–3759. Leuven.
[28] X. Liu, P.A. Meehan, Investigation of squeal noise under positive friction characteristics condition provided by friction modifiers, J. Sound. Vib. 371 (2016) 393–405, https://doi.org/10.1016/j.jsv.2016.02.028.
[29] P.A. Meehan, X. Liu, Modelling and mitigation of wheel squeal noise under friction modifiers, J. Sound. Vib. 440 (2019) 147–160, https://doi.org/10.1016/j.jsv.2018.10.025.
[30] R. Corradi, P. Crosio, S. Manzoni, G. Squicciarini, Experimental investigation on squeal noise in tramway sharp curves, in: Proceedings of the 8th International Conference on Structural Dynamics, EURODYN, Leuven, 2011, pp. 3214–3221.
[31] F. Castellini, L. Faccini, S. Alfi, E. Di Gialleonardo, R. Corradi, G. Squicciarini, D. Thompson, The influence of wheel/rail contact conditions on curve squeal noise: experimental and numerical investigation, in: The Sixth International Conference on Railway Technology: Research, Development and Maintenance, Prague, 2024, https://doi.org/10.4203/ccc.7.13.9.
[32] J. Jiang, R. Dwight, D. Anderson, Field verification of curving noise mechanisms, Notes Numer. Fluid Mech. Multidiscip. Des. 118 (2012) 349–356, https://doi.org/10.1007/978-4-431-53927-8_41.
[33] P.T. Torstensson, A. Pieringer, M. Höjer, R. Nilsson, V. Simonsson, A case study of railway curve squeal radiated from both the outer and inner wheel, Appl. Acoust. 228 (2025) 110327, https://doi.org/10.1016/J.APACOUST.2024.110327.
[34] I. Zenzerović, Time-domain Modelling of Curve squeal: a Fast Model For one- and two-Point Wheel/Rail contact, PhD Thesis, Chalmers University of Technology, 2017.
[35] F. Castellini, L. Faccini, E. Di Gialleonardo, S. Alfi, R. Corradi, Curve squeal of modern tramcars: comparison between independently rotating wheels and solid axles, Int. J. Rail Transp. (2024) 1–18, https://doi.org/10.1080/23248378.2024.2427168.
[36] A.G.J. Macfarlane, I. Postlethwaite, The generalized nyquist stability criterion and multivariable root loci, Int. J. Control 25 (1977) 81–127, https://doi.org/10.1080/00207177708922217.
[37] R.J. Caverly, R. Pates, L.J. Bridgeman, J.R. Forbes, MIMO Nyquist interpretation of the large gain theorem, Int. J. Control 93 (2020) 2326–2335, https://doi.org/10.1080/00207179.2018.1554911.
[38] J.J. Kalker, Three-Dimensional Elastic Bodies in Rolling Contact, Springer Netherlands, Dordrecht, 1990, https://doi.org/10.1007/978-94-015-7889-9.
[39] E.A.H. Vollebregt, User Guide For CONTACT, Rolling and Sliding Contact With friction. Technical report TR20-01, Version 23.2, Vtech CMCC, 2023.
[40] F. Cheli, R. Corradi, G. Diana, A. Facchinetti, Validation of a numerical model for the simulation of tramcar vehicle dynamics by means of comparison with experimental data, J. Comput. Nonlinear. Dyn. 2 (2007) 299–307, https://doi.org/10.1115/1.2754306.
[41] Dimitrios Kostovasilis, Analytical Modelling of the Vibration of Railway track, PhD Thesis, University of Southampton, 2017.
[42] K. Knothe, S. Stichel, Rail Vehicle Dynamics, Springer, Cham, 2016, https://doi.org/10.1007/978-3-319-45376-7.
[43] P. Belforte, F. Cheli, R. Corradi, A. Facchinetti, Software for the numerical simulation of tramcar vehicle dynamics, Heavy Veh. Syst. (2003) 48–69, https://doi.org/10.1504/ijhvs.2003.002434.
[44] O. Polach, A Fast Wheel-Rail Forces Calculation Computer Code, Veh. Syst. Dyn. 33 (1999) 728–739, https://doi.org/10.1080/00423114.1999.12063125.
[45] O. Polach, Creep forces in simulations of traction vehicles running on adhesion limit, Wear. 258 (2005) 992–1000, https://doi.org/10.1016/J.WEAR.2004.03.046.
[46] Z.Y. Shen, J.K. Hedrick, J.A. Elkins, A Comparison of Alternative Creep Force Models for Rail Vehicle Dynamic Analysis, Veh. Syst. Dyn. 12 (1983) 79–83, https://doi.org/10.1080/00423118308968725.
[47] J.J. Kalker, A Fast Algorithm for the Simplified Theory of Rolling Contact, Veh. Syst. Dyn. 11 (1982) 1–13, https://doi.org/10.1080/00423118208968684.
[48] F. Cheli, R. Corradi, A. Facchinetti, A numerical model to analyse the dynamic behaviour of modern tramcars, in: Proceedings of the Mini Conference on Vehicle System Dynamics, Identification and Anomalies, Budapest, 2002, pp. 183–190.
[49] R. Corradi, G. Diana, A. Facchinetti, Sharp curve negotiation analysis of tramcar vehicles with different bogie architectures, Civ.-Comp Proc. 98 (2012), https://doi.org/10.4203/CCP.98.129.
[50] J.P. Pascal, G. Sauvage, The Available Methods to Calculate the Wheel/Rail Forces in Non Hertzian Contact Patches and Rail Damaging, Veh. Syst. Dyn. 22 (1993) 263–275, https://doi.org/10.1080/00423119308969028.
[51] S. Bruni, A. Collina, G. Diana, P. Vanolo, Lateral dynamics of a railway vehicle in tangent track and curve: tests and simulation, Veh. Syst. Dyn. 33 (2000) 464–477, https://doi.org/10.1080/00423114.1999.12063104.
[52] Y.K. Luo, L. Zhou, Y.Q. Ni, Towards the understanding of wheel-rail flange squeal: in-situ experiment and genuine 3D profile-enhanced transient modelling, Mech. Syst. Signal. Process. 180 (2022) 109455, https://doi.org/10.1016/J.YMSSP.2022.109455.